THESIS FOR THE DEGREE OF DOCTOR OF PHILOSOPHY

ADVANCED CHARACTERIZATION TECHNIQUES OF PHOTONIC DEVICES WITH FREQUENCY COMBS

Krishna Sundar Twayana

Photonics Laboratory
Department of Microtechnology and Nanoscience (MC2)
Chalmers University of Technology
Göteborg, Sweden, 2023

Advanced characterization techniques of photonic devices with frequency combs
Krishna Sundar Twayana

ISBN 978-91-7905-852-4
Doktorsavhandlingar vid Chalmers tekniska högskola,
Ny serie nr 5318
ISSN 0346-718X

Photonics Laboratory
Department of Microtechnology and Nanoscience (MC2)
Chalmers University of Technology
SE–412 96 Göteborg
Sweden
Telephone: +46 (0)76–219 58 50

Front cover illustration: Microcomb temporal and spectral profile with equations associated with linear and nonlinear microresonator dynamics.

Printed in Sweden by
Reproservice
Chalmers Tekniska Högskola
Göteborg, Sweden, 2023

Advanced characterization techniques of photonic devices with frequency combs
Krishna Sundar Twayana
Photonics Laboratory
Department of Microtechnology and Nanoscience (MC2)
Chalmers University of Technology

Abstract

Integrated photonics has witnessed remarkable progress in the last decades. Measuring photonic devices in amplitude and phase provides insight into their performance. Swept wavelength interferometry is a prominent technique for the broadband characterization of the complex response. It leverages continuous advances in rapidly tunable laser sources but is prone to systematic errors associated with frequency calibration. This thesis focuses on the non-destructive measurement of ultralow-loss photonic devices using swept wavelength interferometric technique. We overcome issues associated with nonlinear tuning by calibrating the frequency of the laser on the fly with the aid of a frequency comb. We apply the concept to diverse components of relevance including microresonators and spiral waveguides. This technique enables diagnosing waveguides for the loss and potential defects and is instrumental in optimizing device fabrication ecosystems. The measured phase response of microresonators allows for untangling the coupling condition and provides insight into microresonator-waveguide systems. The later part of this thesis covers the linear (stepped and multi-heterodyne) methods for spectral and temporal characterization of frequency combs. The linear heterodyne method provides unprecedented sensitivity and bandwidth range of measurement. In addition, we provide an overview and comparative assessment of the state-of-the-art in the field.

Keywords: frequency combs, microcombs, electro-optic combs, microresonators, waveguides, swept-wavelength interferometry, optical frequency domain spectroscopy, stepped-heterodyne, multi-heterodyne

Publications

This thesis is based on the work contained in the following papers:

[A] K. Twayana, Z. Ye, Ó. B. Helgason, K. Vijayan, M. Karlsson, V. Torres-Company "Frequency-comb-calibrated swept-wavelength interferometry", *Opt. Express*, **29**, 15, 24363-24372, 2021.

[B] K. Twayana, I. Rebolledo-Salgado, E. Deriushkina, J. Schröder, M. Karlsson, V. Torres-Company, "Spectral Interferometry with Frequency Combs", *Micromachines*, **13**, 4, 2072-666X, 2022.

[C] F. Lei, Z. Ye, K. Twayana, Y. Gao, M. Girardi, Ó. B. Helgason, P. Zhao, V. Torres-Company, "Hyperparametric Oscillation via Bound States in the Continuum", *Phys. Rev. Lett.* **130**, 9, 093801, 2023.

[D] K. Twayana, F. Lei, Z. Ye, I. Rebolledo-Salgado, Ó. B. Helgason, M. Karlsson, V. Torres-Company, "Differential phase reconstruction of microcombs", *Opt. Lett.*, **47**, 13, 3351-3354, 2022.

[E] K. Twayana, I. Rebolledo-Salgado, M. Girardi, F. Lei, Ó. B. Helgason, M. Karlsson, V. Torres-Company, "Multi-heterodyne Differential Phase Measurement of Microcombs", *Ultrafast Optical Technologies of the CLEO/Europe-EQEC Conference*, Munich, Germany, 2023.

Related publications and conference contributions by the author, not included in the thesis:

[F] K. Twayana, Z. Ye, Ó. B. Helgason, K. Vijayan, M. Karlsson, V. Torres-Company "Frequency-Comb-Assisted Swept-Wavelength Interferometry" *Conference on Lasers and Electro-Optics Europe & European Quantum Electronics Conference (CLEO/Europe-EQEC)*, Munich, Germany, paper ch.10, 2021.

[G] Ó. B. Helgason, F. R. Arteaga-Sierra, Z. Ye, K. Twayana, P. A. Andrekson, M. Karlsson, J. Schröder and V. Torres-Company, "Dissipative Kerr solitons in photonic molecules", *Nat. Photonics*, 15, 4, 305-310, 2021.

[H] Ó. B. Helgason, Z. Ye, K. Twayana, P. A. Andrekson, J. Schröder and V. Torres-Company "Dark-pulse Kerr combs in linearly coupled microring structures", *Conference on Lasers and Electro-Optics (CLEO)*, San Jose, USA, paper STu3H.5, 2020.

[I] Z. Ye, K. Twayana, P. A. Andrekson and V. Torres-Company "High-Q Si_3N_4 microresonators based on a subtractive processing for Kerr nonlinear optics", *Opt. Express*, 27, 24, 35719-35727, 2019.

[J] Z. Ye, P. Zhao, K. Twayana, M. Karlsson, V. Torres-Company, and P. A. Andrekson. "Overcoming the quantum limit of optical amplification in monolithic waveguides." *Sci. adv.* 7, no. 38 (2021): eabi8150.

[K] Z. Ye, F. Lei, K. Twayana, M. Girardi, P.A. Andrekson, and V. Torres-Company. "Integrated, Ultra-Compact High-Q Silicon Nitride Microresonators for Low-Repetition-Rate Soliton Microcombs." *Laser Photonics Rev.*, 16(3), 2100147, 2022.

[L] Z. Ye, F. Lei, K. Twayana, M. Girardi, P.A. Andrekson, and V. Torres-Company. "Ultralow-loss meter-long dispersion-engineered silicon nitride waveguides." *Conference on Lasers and Electro-Optics (CLEO)*, pp. 1-2. IEEE, 2021.

[M] I. Rebolledo-Salgado, Z. Ye, S. Christensen, F. Lei, K. Twayana, J. Schröder, M. Zelan, and V. Torres-Company. "Coherent supercontinuum generation in all-normal dispersion Si_3N_4 waveguides"". *Opt. Express* 30, no. 6 (2022): 8641-8651.

[N] K. Twayana, F. Lei, Z. Ye, Ó. B. Helgason, I. Rebolledo-Salgado, M. Karlsson, and V. Torres-Company. "Linear Broadband Differential Phase Measurement of Soliton Microcombs". *Conference on Lasers and Electro-Optics (CLEO)*, pp. 1-2. IEEE, 2022.

[O] Z. Ye, F. Lei, K. Twayana, M. Girardi, P. A. Andrekson and V. Torres-Company. "25 GHz soliton microcombs in high-Q Si3N4 racetrack-shaped microresonators". In CLEO: *Applications and Technology*, pp. JTh2F-29. Optica Publishing Group, 2020.

[P] F. Lei, Z. Ye, K. Twayana, Y. Gao, M. Girardi, Ó. B. Helgason, P. Zhao, V. Torres-Company, "Power-efficient hyperparametric oscillation via bound states in the continuum", *Conference on Lasers and Electro-Optics Europe & Applications of Nonlinear Optics of the CLEO/Europe-EQEC Conference*, Munich, Germany, CD-P.1, 2023.

Contents

Abstract **iii**

Publications **v**

Acknowledgement **xi**

Acronyms **xiii**

1 Introduction **1**
- 1.1 Key milestones in Si photonics 1
- 1.2 Precision spectroscopy 4
- 1.3 This thesis 5

2 Laser frequency combs **7**
- 2.1 Optical frequency combs 8
- 2.2 Electro-optic frequency combs 9
- 2.3 Microcombs 11

3 Linear characterization techniques in photonic integration **15**
- 3.1 Swept wavelength interferometry 15
- 3.2 Frequency combs in tuning laser spectroscopy 18
- 3.3 OFDR in waveguides spectroscopy 19

4 High-Q microresonators **23**
- 4.1 Linear dynamics of microresonators 23
  - 4.1.1 Transfer matrix method 24
  - 4.1.2 Spectral characteristics 26
- 4.2 Coupled mode theory 29
  - 4.2.1 Resonance doublet analysis 31

4.2.2 Coupled ring resonators 33
4.3 Microresonator spectroscopy 36
4.4 Dispersion in microresonators 39

5 Microcombs dynamics 45
5.1 Optical field propagating in a nonlinear medium 45
5.2 The Lugiato-Lefever equation and bistability 47
5.3 CW pump to microcomb generation 48
5.4 DKS characteristics 51

6 Linear pulse characterization techniques 55
6.1 Characterization of frequency combs 55
6.1.1 Stepped heterodyne characterization 57
6.1.2 Multi-heterodyne characterization 59
6.1.3 Microcomb characterization 61

7 Future outlook 65

8 Summary of papers 67

Included papers A–E 91

Acknowledgement

I am deeply indebted to my advisor, Prof. Victor Torres-Company, for his unwavering support throughout my Ph.D study. His guidance has been invaluable and has enabled me to develop and expand my knowledge as a researcher. This work would not have been possible without his supervision. I also want to express my sincere gratitude to Prof. Magnus Karlsson for his role as both co-supervisor and examiner. His support, motivation, and insightful comments helped me progress throughout my study. I also thank Prof. Peter Andrekson for allowing me access to the fiber labs and providing me with invaluable insights and knowledge.

I am incredibly grateful to all the brilliant minds in the Photonics laboratory. I have enjoyed our conversations and collaborations immensely. I am thankful to Dr. Attila Fülöp, Dr. Zhichao Ye, and Dr. Òskar Bjarki Helgason for giving up so much of your time to teach me about simulation, device measurement, and lab automation. Dr. Fuchuan Lei has also provided me with invaluable knowledge about the fundamental physics of microcombs and noise sources. A special thanks to Dr. Fuchuan for his invaluable contribution to this work. It has been an extraordinary journey working with Israel Rebolledo Salgado for more than four and a half years. Thank you very much for amity company and for making this arduous journey pleasant and memorable. I would also like to acknowledge Marcello Girardi for your support in programming tools and the interesting discussions we had. Thank you, Yan Gao and Yi Sun for your true collaboration.

Moreover, I am thankful to all the members of the fiber optics lab and optoelectronics lab for contributing to a nice working environment. I am grateful to Dr. Kovendhan Vijayan for his guidance and support in teaching lab instruments and fiber optics. I am also grateful to my fellow students Ekaterina Deriushkina, Zonglong He, Estrella Torres, and Alexander Caut for their cooperation in sharing RF and optical components and discussions. I would like to thank Dr. Ping Zhao for imparting his knowledge on PSA and to Rasmus Larsson and Connor Skehan for fruitful discussions on laser locking and stabilization techniques. Additionally, I would like to thank Gunnel Berggren for her outstanding administrative support.

I had the honor of being a Marie-Sklodowska Curie early-stage researcher in the Innovative Training Network (ITN). I would like to acknowledge Horizon 2020 ITN (GA 812818) and European Research Council (GA 771410) for financing my research and providing opportunities to participate in network conferences and workshops. In the framework of ITN, I have the unique opportunity to visit the Max Plank Institute for the Science of Light and Menlo Systems in Germany. I am thankful to all the members of the Del'Haye Research Group and Dr. Arne Kordts for their kind assistance and valuable insights into their research.

I would like to thank my friends outside the world of photonics but on board with me at different stages of my career. I am thankful to Dr. Santosh Pandit for all the support and fun we have had since my first day in Sweden. My deepest gratitude goes to my brother Badri Narayan Twayana, (who was forcibly disappeared by the state during the civil war in Nepal.) who has been an inspiration to me. Last but not least, I would like to thank all my family and relatives for their endless support and all the love and care that I have received from them.

Krishna Twayana
Göteborg, Sweden
April 2023

Acronyms

CEO	carrier envelope offset
CMOS	complementary metal–oxide–semiconductor
CMT	coupled mode theory
CW	continuous wave
DKS	dissipative Kerr soliton
DOSPM	direct optical spectral phase measurement
DS	dissipative soliton
DUT	device under test
ECDL	external cavity diode laser
EO	electro-optic
EOC	electro-optic comb
FROG	frequency-resolved optical grating
FSR	free spectral range
FWHM	full width at half maximum
FWM	four-wave mixing
GVD	group velocity dispersion
HNLF	highly non-linear fiber
IC	integrated circuit
IM	intensity modulator
LLE	Lugiato-Lefever equation
MI	modulation instability
MLL	mode-locked laser
MZI	Mach-Zehnder interferometer
NLSE	nonlinear Schrödinger equation
OAW	optical arbitrary waveform
OCDR	optical coherence domain reflectometry
OCT	optical coherence tomography
OFC	optical frequency comb
OFDR	optical frequency domain reflectometry

OLCR	optical low-coherence reflectometry
OPO	optical parametric oscillation
ORS	optical reference system
OTDR	optical time domain reflectometry
PIC	photonic integrated circuit
PM	phase modulator
RF	radio frequency
SIMOX	separation by implantation of oxygen
SNR	signal to noise ratio
SOI	silicon-on-insulator
SPIDER	spectral phase interferometry for direct electric-field reconstruction
SPM	self-phase modulation
SWI	swept-wavelength interferometry
TD	time domain
TE	transverse electric
TM	transverse magnetic
XPM	cross-phase modulation

Chapter 1

Introduction

Integrated photonics has been one of the fastest-growing fields in science and technology. Its fundamental physics is analogous to matured fiber optics, which was a key to such rapid progress. The motivation behind integrated photonics is the miniaturization of optical systems and bringing them out from the bulky lab environment into real-world applications. The idea of integrated optics is to achieve an equivalent if not a superior level of complex functionalities and volume production of distributed optical systems on a chip scale. In addition, the integration of optical systems offers improved stability and reliability. Integrated photonics is undergoing a revolution much like microelectronics went through in the 1950s. The trend toward increased functionality, performance, and compactness brings complexity and challenges in the measurement of the devices. The goal of this thesis is to develop advanced measurement techniques to characterize active and passive devices linearly using frequency comb technology.

1.1 Key milestones in Si photonics

Photonics is the science of light, with an emphasis on harnessing photons analogous to electrons in electronics for various applications. The emergence of silicon photonics can be traced back to the 1987s after the demonstration of the electro-optic effect in silicon at the indirect band edge [1]. However, the research in integrated (silicon) photonics gained momentum only from the early 21st century and was adopted in the industry in less than a decade. Integrated photonics is one of the few areas in science ever to be encroached on the global market in the short term.

As of now, the global silicon photonics market is valued at billions of dollars.

The compatibility of silicon photonics with standard complementary metal-oxide semiconductor (CMOS) foundry processes has enabled the rapid progress of Si photonics technology over the past decades. This acceleration was primarily driven by fundamental limitations: power dissipation and bottleneck inherent to the integrated circuits (ICs) in data transmission in data centers. Silicon photonics is slated to resolve the ever-increasing data volume and keep pace with Moore's law. Therefore, this is a holy grail for giant cloud-based IT networks. The high index contrast of silicon on silicon-on-insulator (SOI) platform is ideally suited for the monolithic integration of a range of passive optical components. A Photonics chip (microcomb) under a well-controlled laboratory environment alone can transmit a record 1.84 petabits of data via an optical fiber [2] surpassing the current average internet traffic in the world.

Figure 1.1 depicts some of the key milestones in the evolution of Si photonics. The demonstration of the wafer bonding and Etch-Back technique in 1985 opened up the SOI platform [3]. This method perfectly preserves the crystalline silicon layer unlike the SIMOX (separation by implantation of oxygen) technique [4]. This is the backbone of integrated electronics and photonics technology. The Smart-Cut process of silicon-on-insulator wafers evolves as the de-facto standard of SOI technology [5, 6]. In the mid-1980s, the monolithic integration of Silicon guided waves had been already demonstrated for optoelectronic applications [7]. In its early stage, the SOI waveguides were several micrometers in thickness and width [8]. The SOI wafers technology in [5] allows for the tight confinement of field in the vertical direction, which is key in designing low-loss and sharp-bending waveguides [9]. This is a prerequisite for photonic integration. Interfacing integrated photonics with fiber was an initial hindrance in getting attention from the industries. Due to the fundamental discrepancy in the size of the fiber and waveguide, it was challenging to attain seamless light propagation in and out of the integrated waveguide. This was addressed by delocalizing the light by tapering the waveguide at coupling regions [10] or by highly efficient grating couplers which enable wafer-scale testing of photonic integrated circuits (PICs) [11]. Another milestone in Si photonics is the demonstration of the compatibility of photonics in foundry [12]. However, the lack of a direct bandgap precludes the monolithic integration of active components. Heterogeneous integration is attracting attention in expanding the library of building blocks in silicon photonics [13]. In this regard, active components such as lasers [14], amplifiers [15], and modulators [16] are demonstrated either with chip bonding or direct epitaxial growth. In [17], laser bonded on silicon photonics is reported. Although it lacks the Pockels effect, a silicon-based integrated modulator was demonstrated by carrier injection in [18]. Integrated photonics is not limited to research and state-of-the-art labs. In 2007, Luxtera released a silicon photonics transceiver module with the world's first 40-gigabit optical interconnect to the market [19]. In the following years, integrated photonics exploded in the global market. Photonic integration has made impressive strides in the last decade thanks to the open-access foundry model [20]. This fabless model is facilitated through an integrated ecosystem for the design, development, and manufacturing of customized PICs.

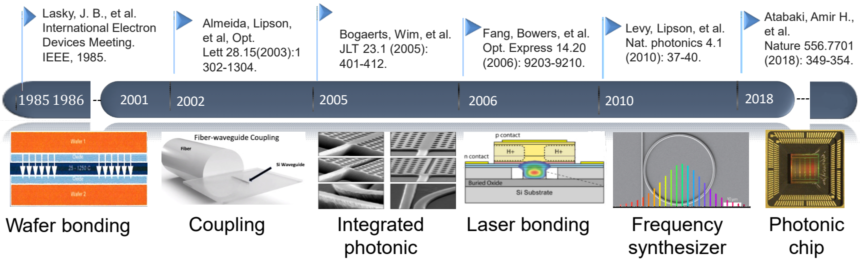

Figure 1.1: Timeline of some of the key milestones in the Si photonics.

The library of building blocks in Si photonics is also expanded to the promising SiN platform [21]. Thin-film Si_3N_4 waveguides with propagation losses comparable to today's state-of-the-art silicon waveguides [22] were demonstrated as early as mid-1980s [23,24]. The wide transparency window from 0.25-8 μm makes it suitable for broadband applications. In addition, the large bandgap (5 eV) and modest Kerr nonlinearity (2×10^{-19} m^2W^{-1}) enable a wide range of nonlinear phenomena. An integrated on-chip multiple-wavelength source in [25] puts forward frequency synthesis and metrology in the silicon-nitride-on-insulator (SiNOI) platform. Multilayer monolithic integration of silicon nitride on silicon platforms unfolds a new avenue in 3D large-scale PICs with both active and passive functionalities [26].

1.2 Precision spectroscopy

Precise characterization of photonic devices is instrumental in the technological advancement and development of many applications. For example, in [27], measurement of the wafer-level group and phase index is reported. This is of great importance in optimizing recipe growth in the subsequent deposition. In [28], the relationship between roughness-induced backscattering with optical parameters, polarization rotation, waveguide geometry, and higher-order mode coupled is illustrated. The characterization of photonic devices uses a laser as a probe and retrieves sensing information that is transduced in changes in amplitude and phase. This requires precise calibration of the laser. In general, the laser frequency is calibrated using auxiliary interferometry. However, this strategy is subject to environmental perturbations and systematic errors attributed to the inherent dispersion. Laser frequency combs as optical rulers are used for accurate frequency calibration of tunable lasers [29].

In order to make accurate measurements of quantities/metrics, a common strategy is to transduce them into frequency. Frequency is the quantity that can be measured with the greatest accuracy. The state-of-the-art comb-referenced spectroscopy can measure a frequency with an accuracy of 20 decimal digits [30]. No other physical quantity can be measured with that level of precision. Arthur Schawlow, the 1981 Nobel Prize winner in physics, advised to "never measure anything but frequency". Earlier precision spectroscopies relied upon cascaded frequency chains that connect the hyper-fine ^{133}Cs microwave clocks to the optical domain. The realization of the optical frequency comb with a mode-locked laser (MLL) enables the direct link between microwave and optical frequencies. In 1997, Theodore W. Hänsch had envisioned a self-referenced frequency comb for a universal optical frequency synthesis [31]. In the late 20$^{\text{th}}$ century, an octave-spanning of an fs pulse using a photonic crystal fiber and f-2f heterodyning enabled absolute frequency synthesis and metrology [32,33]. For this contribution, John L. Hall and Theodore W. Hänsch were honored with half of the 2005 Nobel Prize in physics. In the following years, a new research direction has immersed in the quest of rendering frequency combs on a microscale called 'microcombs'. Microcombs are generated in microresonators by employing the Kerr nonlinear effect from a CW pump laser. The nonlinear interactions give rise to the stimulated parametric mixing that leads to equidistant sidebands, which was first reported in [34]. Microcombs generated in the Si_3N_4 planar platform unravel the prospect of realizing frequency combs in highly compact, robust, and CMOS integration [25].

1.3 This thesis

Measuring integrated photonic devices in amplitude and phase (i.e. complex response) provides insight into their performance. This thesis focuses primarily on the advanced characterization of ultralow-loss microresonators and waveguides (Paper A). We set an external interferometric configuration of the sample for its non-destructive measurement. A self-referenced frequency comb was used as an optical ruler to calibrate the laser used in swept-wavelength interferometry and optical frequency domain reflectometry of the device under test (DUT). The interferometric characterization (Paper B) of photonic devices is instrumental in the use of these devices in various scientific applications. Frequency combs generation (Paper D, E) and hyper-parametric oscillation (Paper C) in microresonators are applications of interest in this thesis. In the next part of the thesis, we reverse our gear and illustrate the use of a (stepwise) tunable laser in differential phase measurement of microcombs (Paper D). We cover the spectral and temporal characterization of microcombs, providing insight into the nonlinear dynamics of the waveforms with unprecedented sensitivity. In addition, we also use a reference comb instead of the tunable laser in paper E. The microcombs characterization is assisted by the electro-optic downconversion technique. Throughout the thesis, we used in-house fabricated Si_3N_4 samples to illustrate these new tools and methods.

Chapter 2 serves as a brief introduction to different types of optical frequency combs. Chapter 3 introduces the basics of swept-wavelength interferometry and self-referenced frequency comb calibration in tunable laser spectroscopy. It also highlights the specific applications in spectroscopy of the devices in detail. Chapter 4 presents the detail about microresonators and their characterization. In chapter 5, the analytical soliton of comb dynamics in the microcavity is briefly discussed, while chapter 6 highlights the linear pulse characterization exemplified in the context of EO-combs and microcombs. Finally, Chapter 7 provides the future outlook.

Chapter 2

Laser frequency combs

Frequency combs are discrete frequency sources that have unleashed enormous possibilities in science and technology. They provide a coherent and bidirectional link between optical and microwave frequencies. Earlier efforts to measure the laser frequency were based on harmonic frequency chains [35]. The rapid advance in mode-locked lasers dramatically simplifies frequency spectroscopy. Their basic principle is mode-locking by either an active element (optical modulator) or a nonlinear passive element (saturable absorber). In 1986, Ti-Sapphire as a broadband gain medium was introduced [36] enabling the generation of a self-mode-locked femtosecond laser [37]. The pulse train corresponds to a series of evenly spaced coherent frequency lines, called a 'frequency comb'. For optical frequency synthesis, the absolute position of the comb lines needs to be traced. In the late 1990s, John L. Hall and Theodor W. Hänsch came up with the revolutionary idea of using an octave-spanning comb and f-2f interferometry, enabling absolute frequency synthesis from radio-frequency atomic frequency references, which stand today as the basis for the SI unit of time. The frequency comb facilitates the most precise timekeeping of an optical atomic clock, which is poised to redefine the time standard [38]. Mathematically, a frequency comb can be described as a train of pulses with an envelope function $A(t)$ modulating a carrier wave. The periodicity of the pulses is ensured by $A(t) = A(t-T)$ with $T = 1/f_r$ denoting the pulse repetition time. The electric field, however, is not periodic given that the carrier wave travels with its phase velocity. The electric field of the frequency comb can be represented according to [39]

$$E(t) = \mathrm{Re}(A(t)\exp^{-j\omega_c t}) = \mathrm{Re}\left(\sum_{n=-\infty}^{\infty} c_n \exp^{-j(\omega_c + n\omega_r)t}\right), \qquad (2.1)$$

with ω_c denoting the carrier frequency and c_n the Fourier series expansion coefficients of $A(t)$. Here, ω_c is not necessarily an integer multiple of ω_r. This causes a global offset (ω_{ceo}) of the modes. The offset is independent of the repetition rate. The frequency of the modes can then be reformulated as $\omega_n = n\omega_r + \omega_{ceo}$ considering $\omega_{ceo} < \omega_r$. In metrology, both the RF frequencies (ω_r and ω_{ceo}) have to be stabilized and referenced to create a frequency ruler. In the following, various types of frequency combs used in this thesis will be discussed briefly.

2.1 Optical frequency combs

Optical frequency combs are a workhorse in modern spectroscopy and metrology [40, 41]. The principle of frequency comb generation relies on mode-locking developed in the mid-1960s after the invention of the laser. Mode locking generates a train of ultra-short optical pulses as a result of constructive interference between coherent lasing modes in the cavity. In the frequency domain, this results in an equidistant spectrum (comb lines) of repetition rate f_{rep} or f_r (used interchangeably in this thesis) as shown in Fig. 2.1. The frequency span of the comb is related to the inverse of the pulse width. However, the pulse envelope and optical carrier wave walk-off introduce an offset frequency referred to as the carrier-envelope offset frequency (f_{ceo} or f_0). As such, the absolute frequency of the comb modes is represented as

$$f_n = nf_{rep} + f_{ceo}, \qquad n \in \mathbb{N}. \qquad (2.2)$$

While f_{rep} is readily measured by beating the comb lines, the estimation of f_{ceo} needs an octave-spanning frequency comb to realize self-referencing via f-2f interferometry. The limited bandwidth of the medium prohibited such measurements until the end of the 1990s. The measurement of f_{ceo} was accomplished with the broadening of mode-locked laser (MLL) via the Kerr effect in a highly non-linear fiber (HNLF) and f-2f interferometry [32,33]. The idea is to frequency double the spectrum and beat with its octave one as shown in the bottom of Fig. 2.1. The self-referenced frequency comb is key for precise laser frequency calibration and broadband spectroscopy of photonic devices which are discussed in chapter 3.

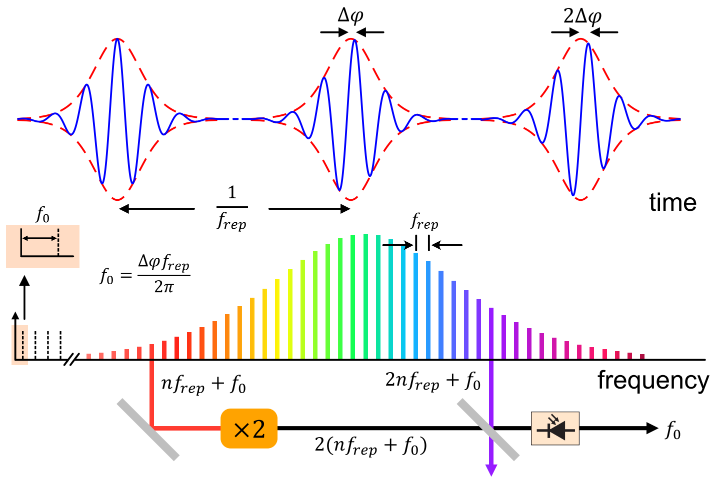

Figure 2.1: Temporal and spectral profile of a femtosecond optical frequency comb. The bottom is the f-2f interferometry for the self-referencing of the comb.

2.2 Electro-optic frequency combs

Electro-optic(EO) modulation is a technique for generating frequency combs. It is a combination of optical and microwave technology. To generate an EO-comb, a CW laser is modulated with an electro-optic modulator using an RF clock. Multiple sidebands are generated, centered around the CW laser and spaced by the RF clock frequency. It is controllable and a CW laser of any wavelength (compatible with the external modulator) is applicable as a light source [42,43]. However, EO-combs had a long-standing problem of high phase noise and low stability as phase noise increases with the comb line number. A self-reference (octave-spanning) EO-comb via nonlinear broadening with sub-optical cycle timing precision demonstrated in [44] could unfold its application in optical atomic clocks and quantum systems.

Electro-optic (EO) central frequency is defined by the seed laser $C(t)$ and spacing by an RF clock. The key element in electro-optic modulation is a phase modulator (PM). The phase-modulated electric field driven by an RF clock (modulating signal) can be modeled as

$$E_{EO}(t) = C(t)\exp^{j\beta\cos(2\pi f_r t)}, \tag{2.3}$$

with β denoting the modulation index and f_r the clock frequency. For simplicity, β can be expressed as normalized driving voltage V_r/V_π. Here, V_r denotes the RF driving voltage and V_π half-wave driving voltage for achieving a phase shift of π. The argument of equation 2.3 defines the frequency swing scaled by a carrier frequency with the maximum bandwidth $2\pi f_r V_r/V_\pi$. The available RF power and practical V_π voltage limit the bandwidth range. The use of multiple PMs is in practice to extend the number of comb lines [45]. It increases linearly with the number of cascaded modulators. The phase between the modulators can be aligned using RF phase shifters to change the shape of the comb spectrum.

The phase modulation in the sideband picture provides more insight into the comb spectrum. The phase modulation in terms of the $\mathrm{n^{th}}$ order Bessel functions $J_n(\beta)$ is

$$E_{EO}(t) = |C(t)| \sum_{n=-\infty}^{\infty} i^n J_n(\beta)\exp(2\pi(f_c + nf_r)t), \tag{2.4}$$

where $J_{-n}(\beta) = (-1)^n J_n(\beta)$ is the n^{th} order Bessel function of the first kind at modulation index β and f_c is the frequency of the seed laser. The phase modulation generates cascaded sidebands centered around f_c with the spacing f_r. As the sideband power is dependent on the Bessel functions of the first kind, the modulation does not generate a flat spectrum. Therefore, an intensity modulator (IM) is often used to flatten or equalize the amplitude of the comb-tones [46]. The IM based on a Mach-Zehnder interferometer driven by the RF signal $V(t) = V_r\sin(2\pi f_r t)$ can be described according to the transfer function as

$$\frac{P_{out}}{P_{in}} = \frac{1}{2}\left[1 + \cos\left(\frac{\pi}{V_\pi}V(t) - \phi\right)\right]. \tag{2.5}$$

The IM is biased at the center of the quasi-linear region. It carves out pulses when the chirp induced by the PM is quasi-linear generating a flat comb (Fig. 2.2(b)) [45]. The "rabbit ears" shape on each side of the flat region is attributed to the strong chirp at the edges. Figure 2.2 shows a schematic diagram, spectral, and temporal profiles of the EO-comb. The field envelope of the EO-comb comprises a train of pulses in the time-domain as shown in Fig. 2.2(c). The temporal phase profile takes the same profile as a modulating RF signal (Fig. 2.2(d)). A convex spectral parabolic phase profile i.e. $\frac{d^2\phi}{d^2\omega} < 0$ (Fig. 2.2(e)) suggests a negative chirp pulse EO-comb. This means the instantaneous frequency decreases with time and the IM is biased at the negative slope of the temporal phase profile (Fig. 2.2(d)). This phase relation between comb-tones indicates that the pulse is chirped and not transform-limited. A transform-limited (narrow train) pulse train can be restored by applying a reverse phase profile (dispersion value) using an appropriate dispersive component such as a waveshaper. Note that the phase profile can be opposite depending on the phase set by the phase shifter. In section 6.1.1, an EO-comb as a comb under test is used to illustrate the heterodyne techniques.

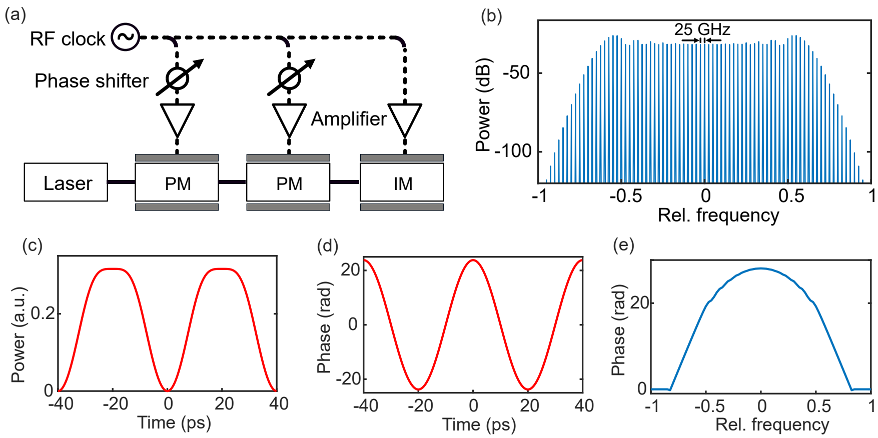

Figure 2.2: (a) EO comb generation setup consisting of two phase modulators and an intensity modulator. The cascaded PM increases the effective modulation depth and the IM flattens the output spectrum. (b) EO comb spectrum of $f_r = 25$ GHz. (c) Pulse profile of the EO comb with a period of $1/f_r = 40$ ps. (d) Phase in time-domain for modulation depth 11.5. (e) Parabolic phase distribution in the frequency domain.

2.3 Microcombs

Microresonator-based Kerr frequency combs ("microcombs") lie at the focus of intense research as an optical source and witnessed significant research progress in the last decade [47, 48]. It is an active research area within chip-scale ultrafast optics and ultrastable lasers, enabling applications in spectroscopy [49] coherent communication [50, 51], optical clock

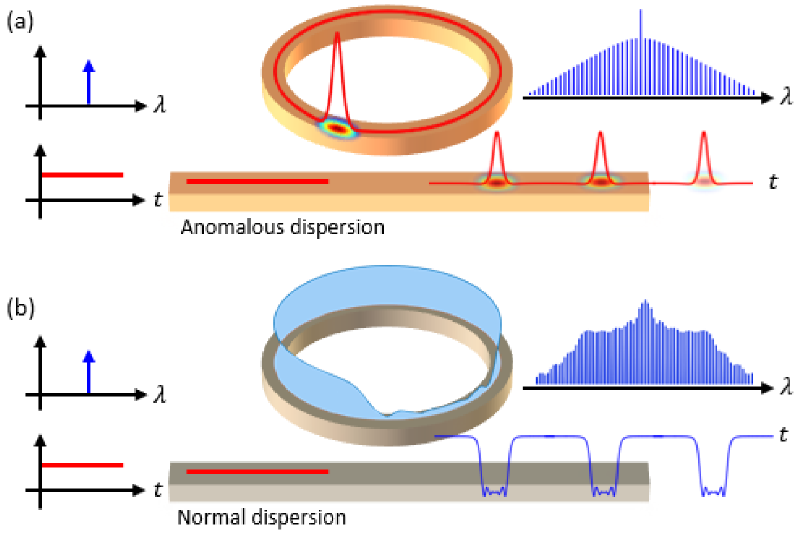

Figure 2.3: Microresonator combs driven by a CW laser. The spectral and temporal profile of (a) dissipative Kerr soliton and (b) dark pulse comb.

generation [52], and optical frequency synthesis [53]. In 2004, optical parametric oscillation (OPO) in a Kerr microresonator was first demonstrated in a silica micro-toroid [54]. The idea of generating frequency combs in microresonators was proposed in [34] and stabilization relative to a microwave signal in [55]. The first demonstration of a microresonator frequency comb in an integrated photonics platform was in silicon nitride (Si_3N_4) [25] and high-index doped silica-glass resonator [56]. The frequency comb generation in a microcomb is initiated by parametric oscillation, followed by cascaded four-wave mixing processes [34]. This process is highly sensitive to the phase of the comb lines. This can lead to coherent waveforms such as dissipative solitons [57], which are self-enforcing optical pulses (wave packets) that circulate in the microcavity as shown in Fig. 2.3(a). In the spectral domain, the pulses coupled out of the cavity form a microcomb with a fixed phase relationship between spectral lines similar to traditional mode-locked lasers. In the cavity, the pulse is formed due to a composite balance of parametric gain and cavity loss together with dispersion and nonlinearity [58]. The parametric gain is maintained at the expense of the input signal power. The intracavity soliton pulse consists of an offset low-power CW state. In contrast, a dissipative pulse in the microcavity also evolves with a high-power CW state in the normal dispersion regime (Fig. 2.3(b)). There is a transition between the low-power and the high-power CW states [59]. These two states are closely related to the CW steady state solution of the bistability. Such an intracavity waveform is known as a platicon or switching wave and the spectrum is called a dark or platicon comb [60]. From knowledge of the comb lines' power and their relative phase, one can fully determine the temporal pulse shape of the microcomb [61] and synthesize the waveform by spatial modulation [62]. Comb dynamics in the microresonators are elaborated in chapter 5. Also, spectral and temporal features are illustrated with simulations and measurements.

Chapter 3

Linear characterization techniques in photonic integration

3.1 Swept wavelength interferometry

Historically, the wave behaviour of light Young's double slit experiment, and interferometry devised by Albert Michelson in 1890 are milestones in advancing the scientific understanding and development of optical technologies. In addition, the invention of the laser in the 1960s and tunable lasers in the following decades drove various interferometry techniques. TD (time domain)-interferometry, spectral domain interferometry, and swept-wavelength interferometry are various interferometry techniques. Optical reflectometry has been a long-standing nondestructive diagnostic tool to probe optical devices or for use in sensing applications. Basically, there are three reflectometric techniques: optical time domain reflectometry (OTDR), optical coherence domain reflectometry (OCDR), and optical frequency domain reflectometry (OFDR). All these techniques are in widespread use. In paper B, we provide a broader context of interferometry by comparing it against state-of-the-art techniques. Depending on the configurations and sources used, there are tradeoffs in terms of sensitivity, resolution, accuracy, speed, and range. OTDR allows measuring the time-resolved distributed reflection of short pulse and propagation losses [63]. It is used for long-distance over kilometers or more and low-resolution spectroscopy. OCDR also known as optical low-coherence reflectometry (OLCR) is essentially a multi-path interferometer using a low-coherence broadband source [64]. It uses a Michelson interferometer operated with a broadband source when the time delay between the arms is nearly equal. It replaces one of the mirrors in the Michelson interferometer with the device under test. A translating mirror is scanned to locate fringes corresponding to reflection points within the DUT (device under test). OCDR with a resolution of 10 μm and dynamic range of greater than 100 dB is demonstrated in [65]. In 1991, optical coherence tomography was first introduced to describe depth-resolved biological imaging using the concept of OCDR [66]. This is time domain (TD-) OCT as envelope fringe pattern is acquired as a function of reference path delay to map reflectivity as a function of transverse plane position.

Swept-wavelength interferometry (SWI) has become a widespread high-precision measurement technique that is applied in diverse applications. In the simplest case, it relies on an interferometric structure based on a broadband sweeping laser where one of the arms contains a device under test (DUT) (see Fig. 3.1). The laser source is swept across the measurement range in the interferometer and the signal is then detected by photodetectors. Interference fringe patterns are acquired as a function of time as the instantaneous frequency of the optical source is tuned. The Fourier transform of this pattern generates the complex impulse of the device under test (DUT). This allows a high-resolution depth-resolved measurement and precise complex transfer function for metrology applications. The diverse array of utilities have been exploited in fiber optics [67], integrated photonics [68], tomography [69], and sensor systems [70].

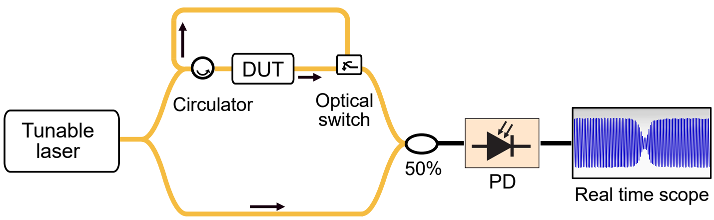

Figure 3.1: Typical Swept wavelength interferometry setup including a DUT. The optical switch configures the transmission or reflection arrangement of the SWI.

Originally, optical SWI was aimed at measuring the reflection in optical fibers [71]. Being analogous to the widely adopted optical time domain reflectometry (OTDR) [72, 73], it was termed optical frequency domain reflectometry (OFDR). In OTDR, distributed reflection is estimated by measuring the propagation delay of short pulses that are back-reflected by weak Rayleigh scattering in fibers. In contrast, OFDR is formed by coherent detection of the interference pattern between optical signals from the test and reference paths by sweeping the laser. The measured beat frequencies can then be mapped into physical distances by knowing the speed of light in the medium.

The general expression of the co-polarized electric field from the arms having time delays τ_1 and τ_2 is expressed as

$$E_1(t) = |E_1|e^{j\phi(t-\tau_1)}, \quad E_2(t) = |E_2|e^{j\phi(t-\tau_2)}, \tag{3.1}$$

where E_i, $i \in 1, 2$ correspond to constant amplitudes. For a linear tuning at a rate v, the instantaneous optical frequency at time t is $v_0 + vt$. The corresponding optical phase is $\phi(t) = 2\pi(v_0 t + vt^2/2)$. The interference of these optical signals on a photodetector in turn generates a photocurrent with constant phase ψ:

$$I(t) = I_0(1 + \cos(2\pi v\tau_0 t + \psi)), \tag{3.2}$$

where, $\tau_0 = \tau_1 - \tau_2$, $I_0 \propto |E_{1,2}|^2$, and ψ as a constant phase offset. This suggests that the delay can be inferred from the beating frequency given the linear tuning rate of the laser. However, the laser sweep is never linear in practice. Since the nonlinear tuning is ingrained in the argument of equation 3.2, it is difficult to disentangle from the relative phase difference of the DUT. Indeed, deviations from a purely linear wavelength sweep cause significant measurement errors and broaden the impulse response function [74]. This issue can be dealt with an active linearization of the tunable laser sources using the self-heterodyne interferometer [75, 76]. However, this technique is inconvenient and compatible only with some categories of tunable sources.

The interference pattern in equation 3.2 can be expressed as a function of instantaneous optical frequency as

$$I(\nu) = I_0(1 + \cos(2\pi\nu\tau_0 + \zeta)), \tag{3.3}$$

with a phase $\zeta = \psi - 2\pi\nu_0\tau_0$. This expression assumes the instantaneous laser frequency does not vary rapidly over τ_0 [74]. The interference pattern is independent of the tuning rate in the frequency domain. In addition, the fringe pattern is periodic with a period $1/\tau_0$. This signal can be used as an external clock to sample an interferogram with a DUT arm of delay time τ_{DUT} [67, 77, 78]. This enables acquiring the fringe pattern free of non-linear laser tuning. However, it requires the Nyquist sampling criteria to be satisfied to avoid aliasing effects i.e. $\tau_{\text{DUT}} \geq 2\tau_0$. Alternatively, an auxiliary interferometer can be used to calibrate the tuning of the laser frequency. The interference pattern is then mapped from the time to frequency axis. However, these methods do not provide absolute accuracy and also suffer from a systematic error. It requires the calibration of the auxiliary interferometer against the dispersion of the delayed arm and operates in a stable condition [77, 79]. Thanks to the optical frequency ruler i.e. frequency comb, the frequency of the tuning laser can be calibrated against these precise and accurate frequency markers. In the interferometric spectroscopes, frequency combs as frequency rulers have been demonstrated for absolute distance measurement [80, 81] and imaging [82]. The relevance of frequency comb in SWI for nondestructive characterization of ultra-low loss photonic devices is highlighted in Paper [A, B] and more detail is discussed in the following sections.

3.2 Frequency combs in tuning laser spectroscopy

The frequency comb as an optical ruler is an invaluable innovation that enables referencing an optical frequency with radio frequency accuracy. In [29], a self-referenced frequency comb was implemented for the spectroscopy of a tunable laser. The broadband precise calibration of the laser with sub-MegaHertz resolution enabled accurate dispersion measurements of microresonators. It is basically an interference between the laser with the comb pulse on a photodetector (Fig. 3.2). This in turn generates RF beatnotes from all the comb lines. The detection of the beat note associated with a particular comb line can be realized by using filters. A narrow bandpass microwave filter of central frequency f_{BP} generates a calibration marker when the scanning laser is $\pm f_{BP}$ away from the comb line. Therefore, the instantaneous laser frequency is calculated as $f_l = nf_{rep} + f_{ceo} \pm f_{BP}$. The sign of the $\pm f_{BP}$ term is related to the direction of the laser scanning. The narrow bandpass RF filters of center frequency f_{BP1} and f_{BP2} generate four beat markers per comb line as shown in Fig. 3.2. This allows a relative frequency calibration of the tuning laser. A reference laser with stable molecular absorption line can be used to resolve the frequency comb mode number (n) knowing the reference laser frequency with a relative accuracy better then half the

f_{ref}. Furthermore, frequency combs allow calibrating cascaded lasers to extend the bandwidth range of spectroscopy while retaining absolute accuracy [83]. However, tuning of the laser in between the calibration markers is approximated by linear or by spline interpolation. The tuning of lasers can be traced more precisely with the aid of the Mach-Zehnder interferometer (MZI). We implemented this technique in the context of swept wavelength interferometer (SWI) and exemplified it with characterizing low loss Si_3N_4 microresonators and spiral waveguides in papers [A, B].

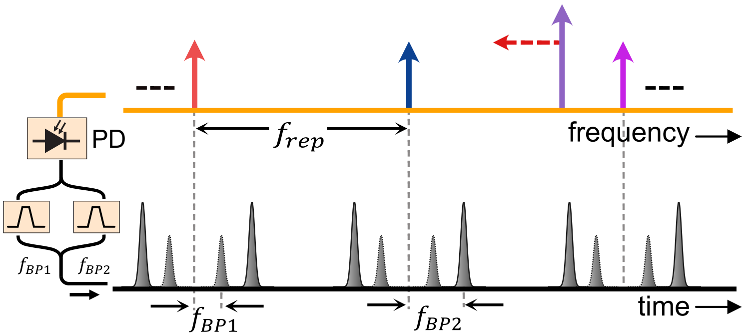

Figure 3.2: Self-referenced comb-assisted calibration of tunable lasers. Frequency comb and mode-hop free tuning laser (top), beat notes detected by two bandpass filters (bottom). The beatnotes are not necessarily equally spaced in time.

3.3 OFDR in waveguides spectroscopy

Attenuation of a field propagating through a waveguide is attributed to inherent material absorption and Rayleigh scattering [28]. In addition, fabrication defects and inevitable side-wall roughness on the waveguide also contribute to the losses. There has been a rigorous effort to completely prevent backscattering using topological interfaces. However, it needs the structure to be designed from materials that break time-reversal symmetry (i.e. unidirectional propagation of photons) without absorbing light [84]. Such a material does not exist as of now.

In integrated photonics, different techniques have been realized to estimate the propagation losses of waveguides [85, 86]. The cut-back method is the simplest way of evaluating the loss. It measures the insertion loss of several waveguides and extracts the propagation loss by calculating the slope versus waveguide length [87]. However, it relies upon uniformity (fabrication yield) of devices, facet consistency, and coupling accuracy. The loss of the waveguide can also be estimated from a ring resonator with an additional penalty of bending loss. In [88], the loss is calculated from the finesse and extinction ratio at the resonances. The intrinsic coupling rate also allows measuring the loss [89]. This method assumes lossless coupling between the waveguide and resonator [90]. Another technique to measure the loss is OFDR, based on the distributed back-scattering of the light. This technique is independent of the facet reflectivity and fiber-waveguide coupling loss. The loss is assumed to be invariant in the propagation direction and constant over the spectral range of the scan. The power difference of reflection peaks can also estimate the loss of the waveguide knowing the facets reflection coefficient [77].

OFDR is a spectral domain reflectometry technique based on a fast-sweeping laser source [91]. It fills the gap in measurement range between OCDR and OTDR. In addition, it provides higher SNR and spatial resolution. It is a spatially resolved highly-sensitive and non-destructive homodyne swept-wavelength interferometry technique. OFDR was initially motivated by the need to characterize distributed reflection in fibers for telecommunication applications [91]. With advances in technology, it has been exploited in the characterization of fiber assemblies [67, 92, 93], integrated photonic devices [94–97], ranging systems [98], and biomedical imaging [69]. In OFDR, the DUT is modeled as a multi-layer medium of group delays $\tau_m (m \in \mathbb{N})$ with respect to the reference arm. As such, the generalized version of equation 3.3 is written as [77, 99]

$$I(\nu) \cong I_0 \left(1 + \sum_m |H_m(\omega)|^2 + 2 \sum_m |H_m(\omega)| cos(2\pi\nu\tau_m + \psi_m(\nu)) \right), \tag{3.4}$$

with the DUT transfer function $H(\nu) = \sum_m |H_m(\nu)| e^{j\psi_m(\nu)}$, which can be retrieved with some Fourier operations. The method is elaborated for an integrated waveguide in paper [A, B]. The Fourier evaluation of a single reflection yields a sinc function [77]. The width of the sinc function determines the fundamental spatial resolution $c/2\Delta\nu$ which is a function of the tuning range $\Delta\nu$.

In OFDR, an auxiliary interferometer has been a long-established method to calibrate the nonlinear tuning of the laser. However, it is subject to external perturbations and systematic error introduced by inherent fiber dispersion. This results in the broadening of the reflection peak and measurement deviation in features of the DUT. Instead of an auxiliary interferometer, in [80, 81], OFDR absolute distance measurement was implemented using a frequency comb as a precise optical frequency ruler. The used frequency comb is a free-running mode-locked laser requiring a sweeping laser to be tuned faster than the CEO drift. In papers [A, B], we demonstrated the relevance of a self-referenced frequency comb for broadband precision in the phase measurement and propagation loss estimation of long spiral waveguides. This non-destructive analysis has helped the group improve the design and fabrication of the waveguides. Figure 3.3 illustrates the reflectivity profiles of the waveguide driven by fundamental quasi-TE and quasi-TM modes. The measured propagation loss is 4.23 dB/m for TE and 4.77 dB/m for TM mode. In both cases, there is a tiny reflection peak (shown by an arrow) along the waveguide segment, which indicates a fabrication defect. The defects were overcome in subsequent fabrications, resulting in a world-record low loss of 1.4 dB/m [100, 101]. Fabrication of such an ultra-low loss meter-long device calls for meticulous stitching error compensation as reported in [102]. The TE mode reflection peak in Fig. 3.3(b) is attributed to either the power coupling from the TM mode along the propagation or residual TE mode in fiber-to-waveguide power coupling.

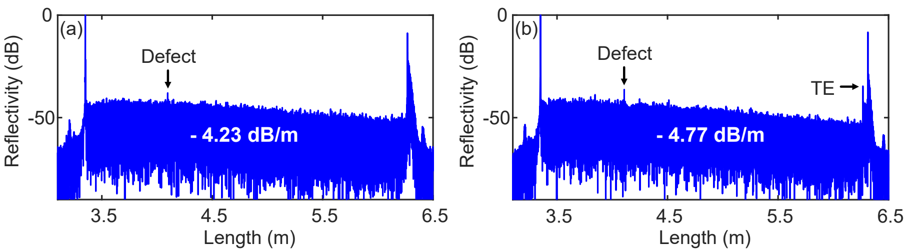

Figure 3.3: OFDR of the waveguide. (a) Spatial reflectivity of the fundamental quasi-TE mode. (b) Spatial reflectivity of fundamental quasi-TM mode.

Chapter 4

High-Q microresonators

A microresonator is a fundamental optical device that has enabled unparalleled functionality in integrated photonics. The light is recirculated and an optical intensity build-up occurs at resonance frequencies. The resonance unfolds if the optical path length is an integer number multiple of the wavelength. This is a fundamental aspect of resonator physics regardless of its geometry and applies to Fabry-Perot etalons [103], microspheres, microtoroids, rod resonators, etc. Microresonators are used in a variety of applications, including modulators [104], optical filters [105], and sensors [106]. The self-injection locking of semiconductor lasers to the high-Q microresonator opens up direction towards integrated sub-hertz linewidth laser [107, 108]. In addition, high-Q microresonators emerge as a workhorse in implementing nonlinear optics at low threshold power. This enables the generation of coherent light sources [54], microwave sources [109], and quantum technologies [110]. The high-Q silicon nitride microresonators are the key building blocks for a large part of this work. This chapter, however, introduces the operating principle of such microresonators (ring resonators) and describes their spectral characterization only in the linear operating regime.

4.1 Linear dynamics of microresonators

The microresonator is a fundamental building block of integrated photonics. Linear dynamics is described for high-Q microresonators operating at low power typically below the sub-milliwatt range. In its simplest form, a microresonator features a waveguide loop (ring) and one or two directional couplers [111]. The evanescent fields of the transverse modes in both waveguides interact and lead to the periodic exchange of power [112]. The coupling strength can be engineered by changing the gap between the waveguides. The coupling of the transverse mode is defined in terms of energy decay rates (coupling rate) or coupling coefficients. There is a direct correspondence between circulating power and energy in the cavity. In the following, we present the transfer matrix method and couple mode theory to discuss various aspects of the microresonators.

4.1.1 Transfer matrix method

The microresonators can be represented in terms of coupling coefficients using the transfer (T) matrix method [113]. This method relates the parameters of the system on one side of a coupler to those on the other. Figure 4.1 illustrates the wave propagating in the forward direction of the N cascaded microresonators. The complex fields normalized to a power at input port E_{in}, output port $E_{\text{out/drop}}$, and cascaded resonators $(a_n, a_n^{'}, b_n, b_n^{'})$ at some notable positions are labeled. Here, we assume the weak point interaction of the fields at the coupling regions.

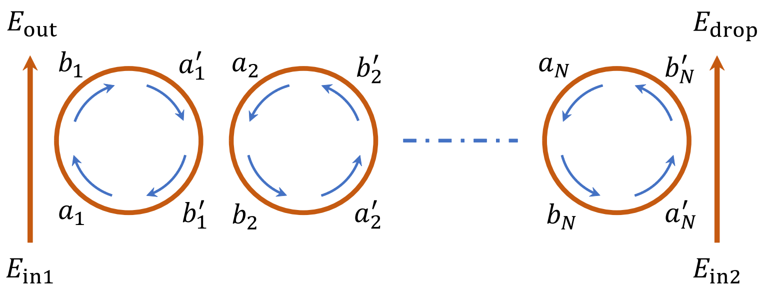

Figure 4.1: Multi-stage traveling wave N resonators with input and output waveguides.

At the coupling region of the cascaded rings, the field interaction is described by a scattering matrix [114]:

$$\begin{bmatrix} b_n^{'} \\ b_{n+1} \end{bmatrix} = \begin{bmatrix} t_{n+1} & \kappa_{n+1} \\ -\kappa_{n+1}^{*} & t_{n+1}^{*} \end{bmatrix} \begin{bmatrix} a_n^{'} \\ a_{n+1} \end{bmatrix}, \tag{4.1}$$

where n = 1, 2,..., N-1 and $|t_{n+1}|^2 + |\kappa_{n+1}|^2 = 1$. t_{n+1} and κ_{n+1} are the dimensionless transmission and outcoupling coefficients respectively. This is also valid for the coupling region at the input and output waveguides.

The transfer matrix $\mathbb{P}$ which relates the fields between the resonators can be derived from these relations and is:

$$\begin{bmatrix} a_{n+1} \\ b_{n+1} \end{bmatrix} = \frac{1}{\kappa_{n+1}} \begin{bmatrix} -t_{n+1} & 1 \\ -1 & t_{n+1}^{*} \end{bmatrix} \begin{bmatrix} a_n^{'} \\ b_n^{'} \end{bmatrix}. \tag{4.2}$$

The field accumulates a phase shift and suffers attenuation as it propagates around the resonator. The propagation of the fields within the ring from one coupling point to another may also be written in terms of a transfer matrix, namely $\mathbb{Q}$:

$$\begin{bmatrix} a_n^{'} \\ b_n^{'} \end{bmatrix} = \begin{bmatrix} 0 & \sqrt{a} e^{-j\beta L/2} \\ \sqrt{a^{-1}} e^{j\beta L/2} & 0 \end{bmatrix} \begin{bmatrix} a_n \\ b_n \end{bmatrix}. \tag{4.3}$$

The amplitude transmission factor per round trip is $a = e^{-\frac{\alpha}{2}L}$ where α is the power attenuation coefficient per unit length and L is the circumference of the ring. The fields between adjacent resonators at the coupling region are obtained by combining equations 4.2 and 4.3.

$$\begin{bmatrix} a_{n+1} \\ b_{n+1} \end{bmatrix} = \mathbb{P}\mathbb{Q} \begin{bmatrix} a_n \\ b_n \end{bmatrix}, \tag{4.4}$$

where $\mathbb{P}\mathbb{Q}$ is the transfer matrix of the unit cell. The expression for the fields at the output of the multi-stage resonator (Fig. 4.1) is obtained by the multiplication of the successive transfer matrixes.

$$\begin{bmatrix} E_{\text{in2}} \\ E_{\text{drop}} \end{bmatrix} = \mathbb{P}_{\text{out}} \mathbb{Q} (\mathbb{P}\mathbb{Q})^{N-1} \mathbb{P}_{\text{in}} \begin{bmatrix} E_{\text{in1}} \\ E_{\text{out}} \end{bmatrix} \equiv \begin{bmatrix} T_{11} & T_{12} \\ T_{21} & T_{22} \end{bmatrix} \begin{bmatrix} E_{\text{in1}} \\ E_{\text{out}} \end{bmatrix}, \tag{4.5}$$

where $\mathbb{P}_{\text{out}}$ and $\mathbb{P}_{\text{in}}$ describe the transfer matrixes between the ring and input/output waveguides. The transfer functions at the output and drop ports for a single input to the first ring resonator ($E_{\text{in2}} = 0$) are:

$$\frac{E_{\text{out}}}{E_{\text{in1}}} = -\frac{T_{11}}{T_{12}} \qquad \frac{E_{\text{drop}}}{E_{\text{in1}}} = T_{21} - \frac{T_{11} T_{22}}{T_{12}}. \tag{4.6}$$

The cascaded ring resonators are used to design various filters and manipulate the resonances selectively [115]. However, in many applications a single-ring configuration (Fig. 4.2) is prevalent. The transfer functions for the add-drop ring configuration derived from equations 4.5 and 4.6 are:

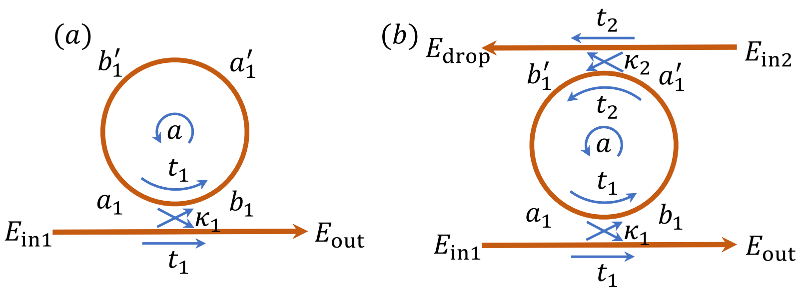

Figure 4.2: A sketch of a single ring resonator. Note 'a' is related to the attenuation factor and with subscript 'a_n' to the field in the ring. a) All-pass ring resonator. b) Add-drop ring resonator.

$$\frac{E_{\text{out}}}{E_{\text{in1}}} = \frac{t_1 e^{j\beta L} - a t_2}{e^{j\beta L} - a t_1^* t_2}, \quad \left|\frac{E_{\text{out}}}{E_{\text{in1}}}\right|^2 = \frac{|t_1|^2 + a^2|t_2|^2 - 2a|t_1||t_2|\cos\phi}{1 + a^2|t_1|^2|t_2|^2 - 2a|t_1||t_2|\cos\phi}, \tag{4.7}$$

$$\frac{E_{\text{drop}}}{E_{\text{in1}}} = \frac{\sqrt{a}\kappa_1\kappa_2 e^{j\beta L/2}}{e^{j\beta L} - a t_1^* t_2}, \quad \left|\frac{E_{\text{drop}}}{E_{\text{in1}}}\right|^2 = \frac{a|\kappa_1|^2|\kappa_2|^2}{1 + a^2|t_1|^2|t_2|^2 - 2a|t_1||t_2|\cos\phi}, \tag{4.8}$$

where $\phi = \beta L + \phi_t$. The net argument of the possibly complex self-coupling coefficients is incorporated in ϕ_t. For an all-pass resonator, the coupling coefficient $|t_2| = 1 - |\kappa_2| = 1$, and equation 4.8 vanishes.

4.1.2 Spectral characteristics

The spectral characteristics of add-drop ring resonators is indicated in Fig. 4.3 according to equations 4.7 and 4.8. The relative positions of the resonances are given by $\beta(\Delta\omega)L = 2\pi\mu$, where μ is the longitudinal mode number. The frequency spacing between two adjacent modes is known as the free spectral range (FSR). It is a function of frequency due to the GVD and higher-order dispersion (to be discussed in more detail in section 4.4).

The individual resonance profile depends on the losses and coupling coefficients. The full width at half maximum (ω_{FWHM}) and depth at the resonance (R_{min}) are the parameters that can be directly extracted from the resonances. These parameters have direct correspondence with the loss and coupling coefficient. To derive the relationship, we expand the

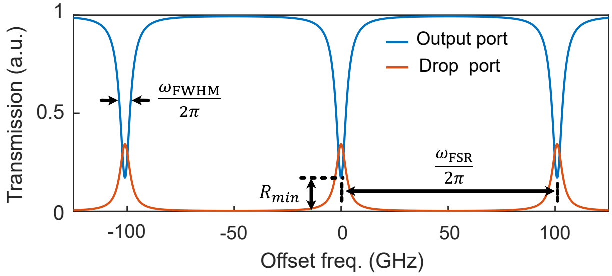

Figure 4.3: Normalized spectra at the output port and drop port with the following parameters: $a = 0.93$, $t_1 = 0.95$, $t_2 = 0.95$, $n_g = 2.1$, $L = 2\pi \times 225\,\mu\mathrm{m}$. The abscissa is offset frequency with regard to the center resonance 1550 nm.

cosine function in equation 4.7 with $\cos\phi \sim 1 - \phi^2/2$. This results in the transmission spectrum as a Lorentzian function in terms of the full width at half maximum (β_{FWHM}) and depth R_{min} of the resonances.

$$\left|\frac{E_{out}}{E_{in1}}\right|^2 = \frac{\phi^2 + R_{\mathrm{min}}(\beta_{\mathrm{FWHM}}/2)^2}{\phi^2 + (\beta_{\mathrm{FWHM}}/2)^2}, \tag{4.9}$$

$$R_{\mathrm{min}} = \frac{(|t_1| - a|t_2|)^2}{(1 - a|t_1||t_2|)^2} \qquad \beta_{\mathrm{FWHM}} = 2\frac{1 - a|t_1||t_2|}{\sqrt{a|t_1||t_2|}} = 2\pi\frac{\omega_{\mathrm{FWHM}}}{\omega_{\mathrm{FSR}}}. \tag{4.10}$$

The numerical solution of equation 4.10 for the all-pass resonator ($t_2 = 0$) allows extraction of the loss (a) and self-coupling (t_1) coefficients [116]. The equations can also be solved analytically. These coefficients are tangled in the equations such that it is difficult to extract them from the transmission spectrum. This is not a problem in the critically coupled case as both coefficients are equal ($a = t_1$). Indeed, prior knowledge of the phase enables untangling these coefficients: $a > t_1$ for overcoupled and $a < t_1$ for undercoupled resonances [117]. The distinct phase profile for the different coupling conditions is depicted in Fig. 4.4.

A vital metric associated with the resonators is the quality factor. It is related to the time constant (field energy decays by a factor of $1/e$ of its initial value) of the resonance field due to the loss (absorption and scattering) and outcoupling. The quality factor (Q) is simply written as the ratio of the resonance frequency ω_0 and the full width at half

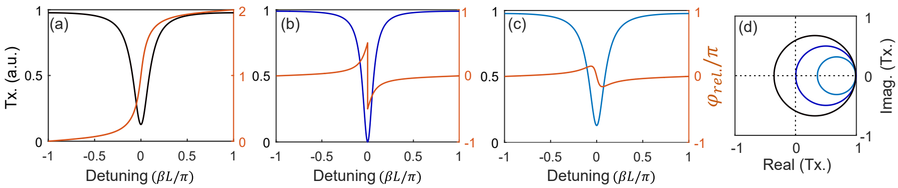

Figure 4.4: Different resonance conditions for the all-pass resonator. Normalized power transmission and phase profile: a) Overcoupling ($a = 0.9, t_1 = 0.8$), b) Undercoupling ($a = 0.8, t_1 = 0.9$), Critical coupling ($a = t_1 = 0.9$). d) Resonances in the complex plane.

maximum.

$$Q = \frac{\omega_0}{\Delta\omega_{\text{FWHM}}} = \frac{\omega_0 n_g L\sqrt{a|t_1|}}{2c_0(1 - a|t_1|)}. \tag{4.11}$$

Assuming the individual low-loss contribution, one can estimate intrinsic (Q_i) and extrinsic (Q_{ex}) quality factors. Also, the loaded quality factor $Q^{-1} = Q_i^{-1} + Q_{ex}^{-1}$.

$$Q_i = \frac{\omega_0 n_g L\sqrt{a}}{2c_0(1-a)}, \qquad Q_{ex} = \frac{\omega_0 n_g L\sqrt{|t_1|}}{2c_0(1-|t_1|)}. \tag{4.12}$$

Figure 4.5 is the Q-factor plot of the high-Q resonator with 9 million mean Q_i. This is an experimental result for a 600×1850 nm^2 silicon nitride microresonator with 217 µm radius and 350 nm gap between the ring and the bus waveguide.

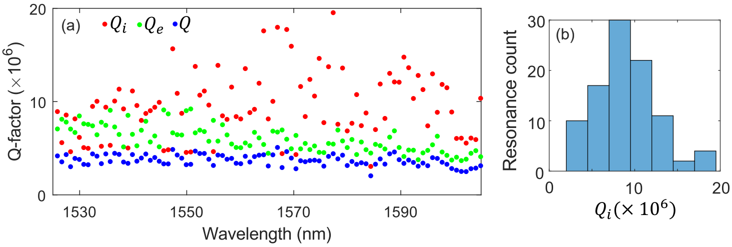

Figure 4.5: a) Quality factor plot of the high-Q resonator of average intrinsic $Q_i = 9$ million. b) Histogram plot of the intrinsic Q.

The intrinsic Q-factor can be directly calculated from the transmission spectrum using [118]:

$$Q_i = \frac{2Q}{1 \pm \sqrt{R_{\text{min}}}}. \tag{4.13}$$

The calculation of Q_i from equation 4.12 is comparable to estimating Q_i using equation 4.13. In equation 4.13, the undercoupled resonance takes the + sign and the overcoupled resonance takes the -sign. The intrinsic and extrinsic coupling rates (discussed below) are estimated by $\kappa_i = \omega_0/(2\pi Q_i)$ and $\kappa_{ex} = \omega_0/(2\pi Q_{ex})$ respectively. The coupling rates have units of 1/s in contrast to the dimensional coupling coefficient κ used in equation 4.1. This allows bridging the metrics of the ring resonator interpreted in different conceptions.

4.2 Coupled mode theory

Coupled mode theory (CMT) is an alternative formalism to describe a weakly coupled system that is consistent with the transfer matrix method [119]. CMT provides insight into the linear dynamics of coupled resonance systems in terms of the photon decay rate, coupling rate, resonance frequency, mode splitting, etc. An energy normalized mode field profile of form $E \sim e^{j\omega_0 t}e^{-t/\tau}$ and its time evolution is described by the differential equation:

$$\frac{dE}{dt} = \left(j\omega_0 - \frac{1}{\tau}\right)E. \tag{4.14}$$

The mode field decays exponentially with a lifetime τ due to the diverse loss mechanisms. This is related to the Q-factor of the resonator and is equivalent to half of the photon (power) decay lifetime. In general, the Q-factor is the ratio between the total energy stored in the cavity and the rate of change of energy per optical cycle (not per cavity roundtrip) [120, 121].

$$Q = \frac{|E|^2}{\left(\frac{d|E|^2}{d|t|}\right) \Big/ \omega_0} = \frac{\omega_0 \tau}{2}. \tag{4.15}$$

In the CMT of resonators, the coupling is defined by an energy coupling rate (κ_{ex}) in a similar way to power outcoupled (κ^2) between the resonator and the waveguide. These coefficients are linked to the field decay time-constant (τ_{ex}) or field decay rate $1/\tau_{ex}$ [122] as:

$$\kappa_{ex} = \kappa^2 \frac{c}{2\pi R} = \frac{2}{\tau_{ex}}. \tag{4.16}$$

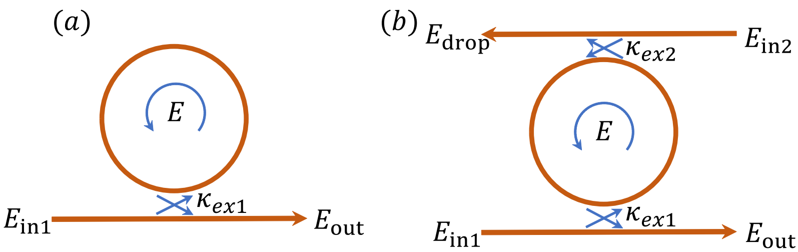

Figure 4.6: A sketch of a single ring resonator. a) All-pass ring resonator. b) Add-drop ring resonator. The field inside the resonator has a unit of the square root of joule and the square root of watt or joule per second for fields outside.

Having this basic understanding of the CMT, we now can investigate the single ring resonator for the transfer functions and spectral characteristics. The CMT equation that describes the resonator mode in the add-drop ring resonator for $E_{in2} = 0$ is:

$$\frac{dE}{dt} = \left(j\omega_0 - \frac{1}{\tau_i} - \frac{1}{\tau_{ex1}} - \frac{1}{\tau_{ex2}} \right) E - j\sqrt{\kappa_{ex1}} E_{\text{in1}}. \tag{4.17}$$

The decay rate $\frac{1}{\tau} = \frac{1}{\tau_i} + \frac{1}{\tau_{ex1}} + \frac{1}{\tau_{ex2}}$ is related to the total power lost in the ring. The intrinsic loss $1/\tau_i$ is attributed to absorption, scattering, and radiation. The loss accounting for the power coupling into the output port is $1/\tau_{ex1}$ and the drop-port is $1/\tau_{ex2}$. The output waves from the waveguides are related to the input field and the resonator mode according to:

$$E_{\text{out}} = E_{\text{in1}} - j\sqrt{\kappa_{ex1}} E \qquad E_{\text{drop}} = -j\sqrt{\kappa_{ex2}} E. \tag{4.18}$$

Equation 4.17 can be solved for E at steady-state assuming an input field $E_{in1}(t) = E_{in1}e^{j\omega t}$ and $E(t) = Ee^{j\omega t}$. Then the transfer function at the output and drop ports can be calculated from equation 4.18.

$$\frac{E_{\text{out}}}{E_{\text{in1}}} = 1 - \frac{\kappa_{ex1}}{j(\Delta\omega) + \omega_{\text{FWHM}}/2} \qquad \left| \frac{E_{\text{out}}}{E_{\text{in1}}} \right|^2 = \frac{(\Delta\omega)^2 + [(\kappa_i - \kappa_{ex1} + \kappa_{ex2})/2]^2}{(\Delta\omega)^2 + [\omega_{\text{FWHM}}/2]^2}, \tag{4.19}$$

$$\frac{E_{\text{drop}}}{E_{\text{in1}}} = -\frac{\sqrt{\kappa_{ex1}\kappa_{ex2}}}{j(\Delta\omega) + \omega_{\text{FWHM}}/2} \qquad \left| \frac{E_{\text{drop}}}{E_{\text{in1}}} \right|^2 = \frac{\kappa_{ex1}\kappa_{ex2}}{(\Delta\omega)^2 + [\omega_{\text{FWHM}}/2]^2}, \tag{4.20}$$

where $\omega_{\text{FWHM}} = \kappa_i + \kappa_{ex1} + \kappa_{ex2}$ and $\Delta\omega = \omega - \omega_0$. κ_i is called intrinsic coupling rate and κ_{ex} external coupling rate. Equations 4.19 and 4.20

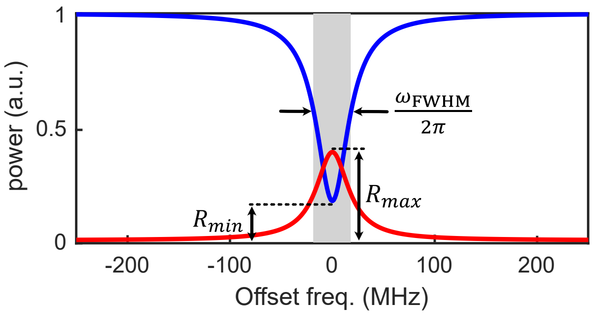

Figure 4.7: Lorentzian shaped spectral response (blue for output and red for drop ports) of the add-drop ring resonator for $\kappa_i = 80/2\pi$ MHz, $\kappa_{ex1} = 70/2\pi$ MHz, and $\kappa_{ex2} = 60/2\pi$ MHz.

are equivalent to the Lorentzian function of full width at half maximum ω_{FWHM} and

$$R_{\text{min}} = \frac{(\kappa_i - \kappa_{ex1} + \kappa_{ex2})^2}{(\omega_{\text{FWHM}})^2}, \qquad R_{\text{max}} = \frac{4\kappa_{ex1}\kappa_{ex2}}{(\omega_{\text{FWHM}})^2}. \tag{4.21}$$

It is evident from equation 4.21 that the transmitted power vanishes at ω_0 for $\kappa_{ex1} = \kappa_i + \kappa_{ex2}$. All the input power at ω_0 either routes to the drop-port and/or dissipate in the ring. This is a necessary condition for critical coupling to occur. An inequality in the critical coupling condition results in undercouple ($\kappa_{ex1} < \kappa_i + \kappa_{ex2}$) or overcouple ($\kappa_{ex1} > \kappa_i + \kappa_{ex2}$) resonance.

4.2.1 Resonance doublet analysis

In microresonators, distributed backscattering is inevitable due to the sidewall roughness along the circumference. In addition, the localized discontinuities at the coupling region account for the lump backscattering [123]. The coherent build-up of backscattered/reflected light excites the clockwise (cw) mode. The coupling between degenerate cw and counterclockwise (ccw) modes distorts the ideal Lorentzian profile and eventually leads to resonance-splitting [123, 124]. The resonance splitting is different for each resonance due to the stochastic nature of backscattering. Figure. 4.8 shows a ring resonator with the ccw (E_+) and cw (E_-) modes. Here we exclude a drop-port to simplify the system of equations.

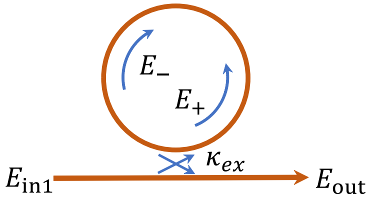

Figure 4.8: A sketch of a single ring resonator with cw and ccw modes.

The coupled-mode equations describing such a system are written as:

$$\begin{aligned}
\frac{dE_+}{dt} &= \left(j\omega_0 - \frac{1}{\tau_i} - \frac{1}{\tau_{ex}}\right) E_+ - j\frac{\kappa_c}{2}E_- - j\sqrt{\kappa_{ex}}E_{\text{in1}}, \\
\frac{dE_-}{dt} &= \left(j\omega_0 - \frac{1}{\tau_i} - \frac{1}{\tau_{ex}}\right) E_- - j\frac{\kappa_c}{2}E_+, \\
E_{out} &= E_{in1} - j\sqrt{\kappa_{ex}}E_+,
\end{aligned} \tag{4.22}$$

where E_+ and E_- are the complex fields of the counter-propagating modes, and κ_c is the complex coupling rate between cw and ccw fields. Equation 4.22 can be solved for the time-dependent input $E_{in1}(t) = E_{in1}e^{j\omega t}$, ccw mode field $E_+(t) = E_+e^{j\omega t}$, and cw mode field $E_-(t) = E_-e^{j\omega t}$. The transfer function of the resonance spectrum is obtained by rewriting the equations considering the steady-state counter-propagating mode fields.

$$\frac{E_{\text{out}}}{E_{\text{in1}}} = \frac{\kappa_i^2 - \kappa_{ex}^2 - 4(\Delta\omega)^2 + i4\kappa_i(\Delta\omega) + \kappa_c^2}{(\kappa_i + \kappa_{ex})^2 + \kappa_c^2 - 4(\Delta\omega)^2 + i4(\kappa_i + \kappa_{ex})(\Delta\omega)}, \tag{4.23}$$

The decay rate is substituted by the coupling rate from equation 4.16. For $\kappa_c = 0$, this resonance profile is equivalent to the Lorentzian distribution and the intensity transfer function is identical to equation 4.19.

The distributed coupling rate with $\kappa_c^2 > |\kappa_i^2 - \kappa_{ex}^2|$ excites symmetric resonance doublets with equal linewidths Fig. (4.9(a)). There exist two loops in the complex plane and the origin is always out of the resonance contour (4.9(b)).

In practice, the resonance doublet can have various asymmetric lineshapes (observed in paper A). This is attributed to the lossless dissipative (indirect via radiation) coupling [125], typically, due to the coupler-induced backscattering [123]. We incorporate this effect into CMT by defining a complex coupling rate. The real $\kappa_{c,R}$ and imaginary $\kappa_{c,I}$ terms

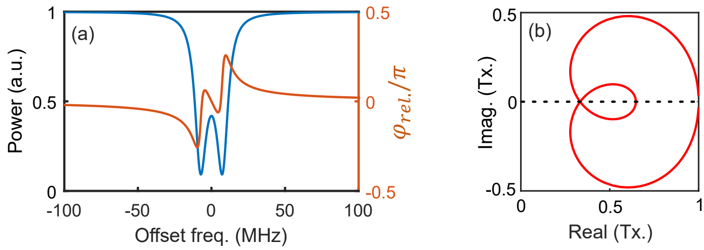

Figure 4.9: Symmetric resonance split for $\kappa_i = 20/2\pi$ MHz, $\kappa_{ex} = 40/2\pi$ MHz, $\kappa_c = 100/2\pi$ MHz. a) Transmission response and phase profile. b) Phasor diagram plot.

define the resonance splitting and asymmetry in the split resonances respectively. The linewidth of one split resonance gets narrower, while the other resonance gets broader due to the $\kappa_{c,I}$. This is analogous to the via-the continuum coupling term described in paper C but the modes share a common decay channel in counterpropagating directions. Figure. 4.10 shows an asymmetric split of the resonance.

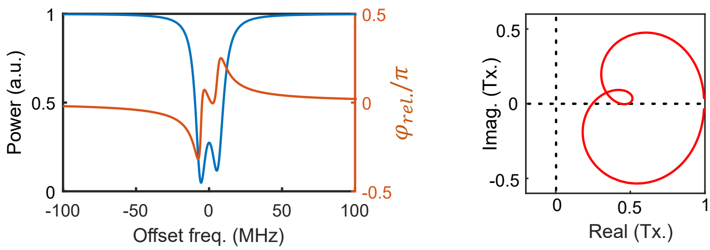

Figure 4.10: Asymmetric resonance split for $\kappa_i = 20/2\pi$ MHz, $\kappa_{ex} = 40/2\pi$ MHz, $\kappa_c = (80 + j5)/2\pi$ MHz. a) Transmission response and phase profile. b) Phasor diagram plot.

4.2.2 Coupled ring resonators

Introducing linear coupling between different rings enables several functionalities in photonics (such as higher-order filters [105] and microcombs [126]). Analogous to the band splitting in atomic physics, the linear coupling results in the avoided mode crossing in coupled ring resonators system also known as a photonic molecule [127]. The splitting of longitudinal modes can also be generated by the interaction of the cw and ccw modes in a single resonator as discussed in the previous section.

It is hard to customize the splitting in practice due to the fact that the ccw mode is excited by random perturbations on the ccw traveling wave. Cavities in cascade, however, allow engineering the coupling strength and tune resonances independently. Such photonic molecules in normal and anomalous dispersion are used in papers [D, E].

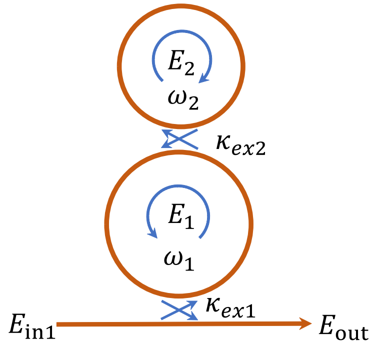

Figure 4.11: . A sketch of linearly coupled ring resonators.

The time evolution of the mode fields in the cavities of the coupled systems is written as:

$$\begin{aligned}\frac{dE_1}{dt} &= \left(j\omega_1 - \frac{1}{\tau_i} - \frac{1}{\tau_{ex1}}\right) E_1 - j\frac{\kappa_{ex2}}{2}E_2 - j\sqrt{\kappa_{ex1}}E_{\mathrm{in1}}, \\ \frac{dE_2}{dt} &= \left(j\omega_2 - \frac{1}{\tau_i}\right) E_2 - j\frac{\kappa_{ex2}}{2}E_1, \\ E_{out} &= E_{in1} - j\sqrt{\kappa_{ex1}}E_1,\end{aligned} \tag{4.24}$$

with the mode fields E_1 and E_2 and the uncoupled resonance frequencies ω_1 and ω_2. The steady-state solution of these equations for the time-dependent input $E_{in1}(t) = E_{in1}e^{j\omega t}$ and resonators mode fields $E_i(t) = E_i e^{j\omega t}$ results in:

$$\frac{E_{\mathrm{out}}}{E_{\mathrm{in1}}} = 1 - \frac{\kappa_{ex1}}{\left(j\Delta\omega_1 + \frac{\kappa_i}{2} + \frac{\kappa_{ex1}}{2}\right) + \frac{\frac{\kappa_{ex2}^2}{4}}{j\Delta\omega_2 + \frac{\kappa_i}{2}}}. \tag{4.25}$$

The resonance locations of the coupled system are given by [112]:

$$\omega^{\pm} = \frac{\omega_1 + \omega_2}{2} \pm \sqrt{\left(\frac{\omega_1 - \omega_2}{2}\right)^2 + \left(\frac{\kappa_{ex2}}{2}\right)^2}. \tag{4.26}$$

We use this equation in Fig. 4.12(a) to illustrate the mode crossing using $\kappa_{ex2}/2\pi = 400$ MHz. The superposition of the orthogonal modes (ω_1 and ω_2) of the unperturbed system generates the supermodes $\omega^{\pm}$. The supermodes spectra in Fig. 4.12(b) are rendered according to equation 4.25 using $\kappa_{ex2}/2\pi = 400$ MHz, $\kappa_{ex1}/2\pi = 10$ MHz, and $\kappa_i/2\pi = 2$ MHz. We set the resonance of the first cavity (ω_1) as a reference (ω_0) and the second cavity resonance (ω_2) offset by an integer multiple of 1 GHz. In practice, the thermal optic effect readily allows the cavity resonance tuning. The avoided mode-crossing enables localized dispersion engineering to realize the phase-matching for initializing a (dark-pulse) comb in a normal dispersion regime [126,128]. We used such a configuration in paper B to illustrate the differential phase measurement technique of the comb.

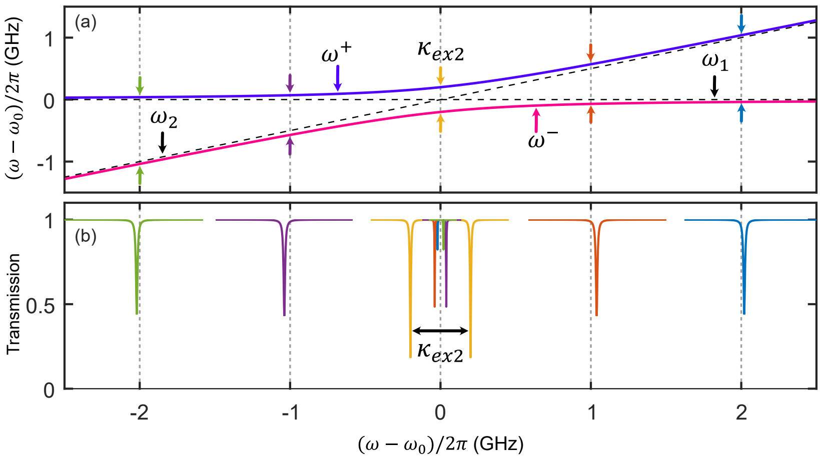

Figure 4.12: Interaction between resonances of the linearly-coupled cavities. a) Illustration of the avoided mode-crossings. The uncoupled modes ω_1 and ω_2, coupling rate κ_{ex2}, and supermodes ω^+ and ω^- are labeled. The resonance of the first cavity ω_1 is considered as a reference mode. b) Supermodes distribution of the resonances at the location marked in a) with arrows of identical colors. The spacing between the coupled resonances complies with the supermodes gap in a). At the mode crossing point, the distance between the supermodes $(\omega^+ - \omega^-)/2\pi = \kappa_{ex2}$.

4.3 Microresonator spectroscopy

Self-referenced frequency combs for wavelength calibration of tunable lasers is a prominent technique in a broadband high-precision spectroscopy of microresonators [29, 83]. It enables precisely resolving the frequency axis of the longitudinal modes and retrieving accurate dispersion values of different transverse mode families [29,129]. The dispersion of microresonators results in a relative offset of the resonances from the equidistant frequency grid. Other properties of the resonances are embedded in their profile [117]. As the resonance profile is invariant to the commutation of the coupling rates, the coupling condition cannot be distinguished [130]. In [131], the resonance condition is identified assuming weak wavelength dependent loss. It is possible to untangle the coupling condition by measuring the phase responses of the resonances [117]. The resonance phase profile can be measured with a network analyzer by sweeping microwave modulation frequency [128]. However, the measurement range is restricted within the microwave sweeping range per scan. In [132], the phase profile of the resonances was extracted by fitting an interference pattern of a resonator coupled to a balanced MZI. In papers [A, B, C], we demonstrated the characterization in both amplitude and phase of the microresonator configured in unbalanced MZI calibrated with a self-reference comb. The idea is to detect the sensing information transduced in the interference pattern by scanning the interferometer using a mode-hope-free tuning laser. The acquired interference pattern is mapped to the frequency axis with the help of a fiber laser frequency comb. The Fourier transfer of frequency discretized interference pattern generates an impulse response as shown in Fig. 4.13. The reference impulse (inset) is attributed to the interference of the probe signal without passing through the resonator cavity. The inverse Fourier transform from those traces gives the reference ($\mathcal{H}_{ref}$), and the overall ($\mathcal{H}_{tot}$) transfer function of the system. Therefore, the equivalent complex transfer function of the device under test is $\mathcal{H}_{ring} = \mathcal{H}_{tot}/\mathcal{H}_{ref}$. The retrieval of other important properties of the resonances is illustrated below.

The smoothness of the resonance spectrum is limited by the spectral resolution and the overall noise in the system. As such, a parametric fitting is prevalent in extracting the properties of the resonances. The lineshape fitting model is applied to extract the properties of the resonances. The Lorentzian model is commonly used for the transmission spectrum fitting to retrieve the characteristic parameters of the resonances [118]. This fitting model allows unambiguous identification of

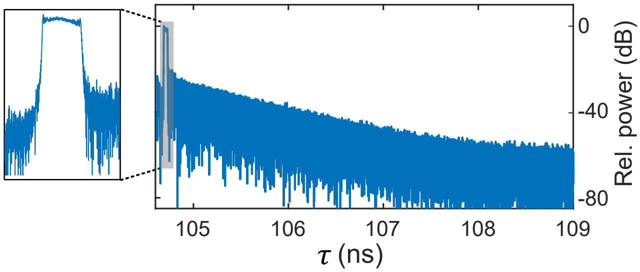

Figure 4.13: Impulse response of the SWI of the microresonator as a function of time delay. The microresonator properties are embedded in the inclining relative power trace. The zoom-in section is the reference impulse response of the SWI without the ring.

the coupling parameter with the aid of the phase profile [116]. The intrinsic and extrinsic coupling rates are estimated as: $\kappa_i = \omega_0/(2\pi Q_i)$ and $\kappa_{ex} = \omega_0/(2\pi Q_{ex})$ respectively. The Lorentzian lineshape fitting of some of the resonances is shown in the first row of Fig. 4.14. The resonances feature no visible splitting, however, there is a noteworthy remanent of the counter-propagating mode coupling. The Lorentzian fitting discussed above disregards this effect. Therefore, coupled-mode theory (CMT) in the time domain is widely adopted to retrieve the characteristics parameters of the resonances [124, 133].

A parametric fitting of equation 4.23 at $\kappa_c = 0$ allows direct retrieval of the κ_i and κ_{ex}. It is clear that these coupling rates are interchangeable. However, from the prior knowledge of the coupling condition, the coupling rates are untangled as $\kappa_{ex} > \kappa_i$ for the overcoupled and $\kappa_{ex} < \kappa_i$ for the undercoupled regime. Figure 4.14 shows that the Lorentzian fitting (first row) is in concurrence with the CMT fitting of the resonances for κ_c=0 (second row). The above fittings neglect the contribution of κ_c on the FWHM and attribute its implications on the κ_i and/or κ_{ex}. As such, it overestimates the net coupling rates and underestimates the total Q-factor. Therefore, it is of utmost importance to consider κ_c in the parametric fitting.

In general, the extended CMT fitting considers a complex counter propagating mode coupling rate $\kappa_c = \kappa_{c,R} + i\kappa_{c,I}$. An asymmetric (symmetric) resonance is observed for complex (real) κ_c. The split mode resonance fitting of the resonances is shown in the third row of Fig. 4.14. The complex part of κ_c is not highlighted in the figure as the resonances are quite symmetric without a visible doublet. All the resonances fit well.

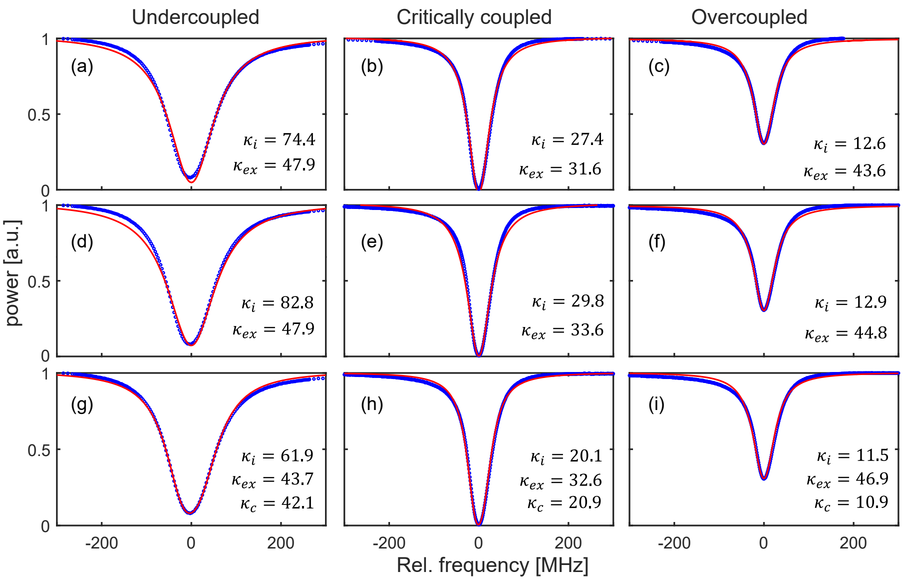

Figure 4.14: Normalized transmission spectra (blue) and parametric fitting profiles (red) of undercoupled, critically coupled, and overcoupled resonances in columns. Each column has identical raw data at different locations of the resonance spectrum. The coupling rates have a unit of MHz. (a-c) Lorentzian lineshape fitting model. (d-f) Parametric coupled mode resonance fitting neglecting ccw mode coupling. (g-i) Parametric coupled mode resonance fitting considering ccw mode coupling.

Remarkably, resonance fitting and coupling rates in the third column of Fig. 4.14 are equivalent. This is due to the fact that the resonance has weaker κ_c. However, there is a significant disparity in the coupling rates when the κ_c is stronger (the first column in Fig. 4.14).

Paper [A], presents the first demonstration of empirical IQ plane parametric fitting of the resonances. Having an extra fitting dimension (phase), this fitting is more robust and returns an unambiguous and consistent set of coupling rates. The IQ plane parametric fitting of the single and split resonance traces are illustrated in Fig. 4.15 (a) and (d). The normalized resonance power and phase profile obtained from the complex plane fitting (red traces) are shown along with the corresponding measured profiles (blue traces). This fitting generates the coupling rates, in Fig. 4.15 (b) that absolutely satisfy the critical coupling condition i.e. $\kappa_c \sim \sqrt{|\ \kappa_{ex}^2 - \kappa_i^2\ |}$. This is commensurate with the resonance transmission and phase profile. In Fig. 4.15(d), the inner loop is attributed to

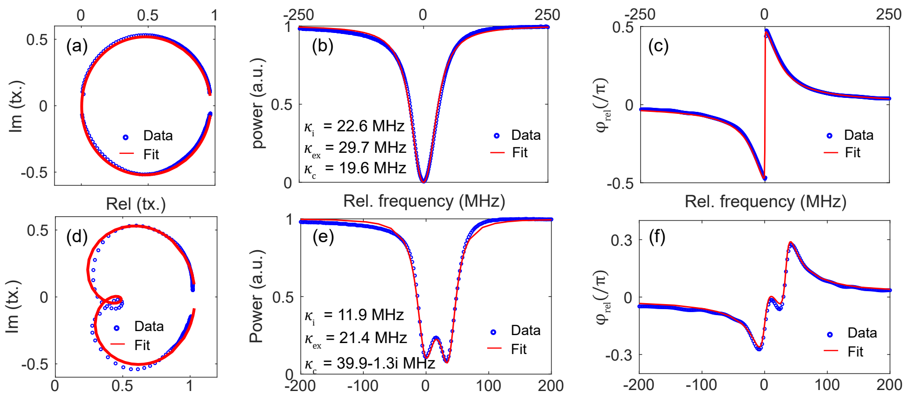

Figure 4.15: IQ plane fitting of the resonances (blue measured and red fitting). Critical coupled resonance (a) IQ plane plot, (b) resonance transmission profile, (c) Phase profile. d-f) idem to a-c) but for asymmetric split resonance.

the resonance split. The resonance doublet with asymmetric resonance lineshape and the corresponding phase profile are shown in Fig. 4.15(e) and (f) respectively.

4.4 Dispersion in microresonators

The measurement of optical properties discussed above is highly dependent on the resonance lineshape. A small relative frequency offset of the resonances will not impact the extraction of the resonance properties. Therefore, absolute accuracy is not that critical for extracting those parameters. For our high-Q microresonators, the resonance linewidth is below 50 MHz. This brings to us the idea of using a traditional auxiliary interferometry technique in laser frequency calibration. It is fairly reasonable to assume a constant group delay of fiber used in the auxiliary interferometry for such narrow linewidth resonances distributed across the transmission spectrum. We verified that the extraction of the resonance properties using auxiliary interferometry matches well with the frequency comb calibration technique. In contrast, the relative frequency offset of the resonance frequency due to the systematic error (frequency-dependent group delay) of the auxiliary interferometer causes a signification deviation in the dispersion measurement of microresonators. Therefore, the precise frequency calibration of the tuning laser is of interest in the dispersion measurement. The frequency comb-assisted laser frequency calibration is highly relevant in this context [29]. Dispersion measurement also demands a high spectral resolution as the linewidths and the mode spacing deviations are in the order of kHz and MHz. The spectral resolution depends on the bandwidth scanning range and the memory depth of the acquisition system.

In microresonators, resonance occurs if the phase shift of field after one roundtrip is an integer multiple of 2π, i.e. $\beta(\omega_\mu) - \beta(\omega_0) = 2\pi\mu/L$; $\mu \in \mathbb{Z}$. Here, ω_0 is the reference resonance frequency and ω_μ is the μ^{th} resonance, counted from ω_0. This resonance condition under the Taylor expansion of the frequency dependent propagation vector β is

$$(\omega_\mu - \omega_0)\beta_1(\omega_0) + \frac{(\omega_\mu - \omega_0)^2}{2}\beta_2(\omega_0) + \frac{(\omega_\mu - \omega_0)^3}{6}\beta_3(\omega_0) + ... = \frac{2\pi\mu}{L}, \tag{4.27}$$

where β_0 is the phase velocity, β_1 is the group velocity, and β_2, β_3,... are dispersive orders. The dispersion parameters are extracted by a polynomial fit for all the resonances with respect to the reference resonance ω_0. The evaluated β_n, $n = 1, 2, 3, ...$ at ω_0 can be used to calculate n$^{\text{th}}$-order dispersion as a function of ω:

$$\frac{d^n\beta}{d\omega^n} = \sum_{k\geq 0} \frac{1}{k!}\beta_{(n+k)}(\omega_0)(\omega - \omega_0)^k. \tag{4.28}$$

The dispersion can also be described as the variation of FSR over resonance frequencies. This is a common metric for describing the spectral extension and shape of microresonator frequency combs [134]. Due to the higher order dispersion acts upon the GVD, dispersive waves induce at $D_{int} = 0$. This is a key feature of generating an octave-spanning comb in microresonators [135]. The μ^{th} order resonance frequency ω_μ relative to ω_0 is

$$\omega_\mu = \omega_0 + \sum_{j=1} \frac{D_j\mu^j}{j!} = \omega_0 + D_1\mu + \frac{1}{2!}D_2\mu^2 + ... = \omega_0 + D_1\mu + D_{int}, \tag{4.29}$$

where, $D_1/2\pi$ corresponds to a mean FSR and D_{int} is a deviation of the resonance frequency from an equidistant resonance grid attributed to all dispersive terms ($D_2/2\pi, D_3/2\pi, ...$ in Hz). These coefficients are mutually related to the coefficients in equation 4.27 as $\beta(\omega_0 + \sum_{j=1} \frac{D_j\mu^j}{j!}) - \beta(\omega_0) = 2\pi\mu/L$. It can be established by Taylor expansion about ω_0 and equating the coefficients of μ^j, that we obtain

$$\beta_1 = \frac{2\pi}{D_1 L}, \qquad \beta_2 = -\frac{2\pi}{L}\frac{D_2}{D_1^3}, \qquad \beta_3 = -\frac{2\pi}{L}\frac{D_3}{D_1^4}, ... \tag{4.30}$$

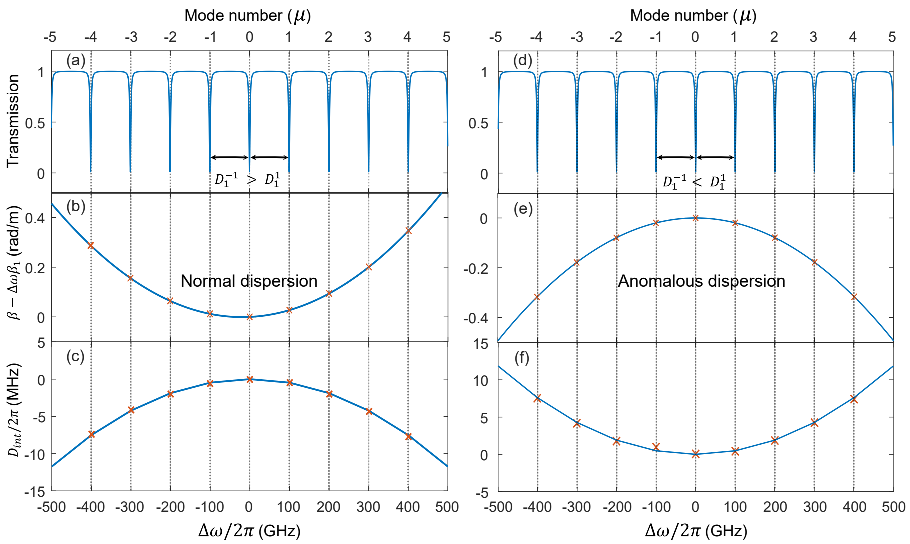

Figure 4.16: Zoom of dispersive ring resonator spectrum simulated from 1535 nm to 1565 nm. a) Transmission profile plot according to equation 4.7 using parameters $a = 0.99$, $t_1 = 0.96$, $t_2 = 0.96$, $L = 2\pi \times 238\,\mu\text{m}$, $n_g = 2.1$, $\beta_1 = 6$ ps/km, $\beta_2 = 100$ ps^2/km with a reference mode μ_0 at $\sim$ 1550 nm and record length of five million. The normal GVD causes a reduction of the FSR towards higher resonance frequencies. b) Taylor expansion of the propagation constant without the effects of β_0 and β_1. c) Integrated dispersion plot. The retrieved dispersion from the resonance frequencies is $\beta_2 = 99.6 \pm 0.5$ ps^2/km. d-f) idem to a-c) but for $\beta_2 = -100$ ps^2/km. The retrieved dispersion value is $\beta_2 = -100.6 \pm 0.5$ ps^2/km.

In the following, we discuss the dispersion and its implication on the resonance spectrum of the microresonator. Figure 4.16 shows the simulation of the add-drop ring resonator spectra incorporating the dispersion effect. We use a Taylor series expansion of the propagation vector for $\phi = \beta L$ in equation 4.7. The GVD causes the mode numbers to appear at uneven spacing. The FSR decreases (increases) with frequency for the normal (anomalous) dispersion. This is not evident from the transmission plot because of the small GVD and few longitudinal modes. However, the concave (convex) propagation vector and convex (concave) integrated dispersion plot suggests the normal (anomalous) dispersion of the ring resonator.

We evaluated the importance of spectral resolution in dispersion calculation from the transmission spectra in Fig. 4.16. To do so, we define a half million data points (memory depth). This results in a random offset of the resonance frequency dips. The evaluated dispersion turns out to be more uncertain and off from the actual value, $\beta_2 = 98 \pm 5$ ps^2/km for normal and $\beta_2 = -101 \pm 5$ ps^2/km for anomalous dispersion. To reduce the effect of limited spectral resolution, we consider the resonance frequency for the dispersion calculation from the resonance line shape model in all our papers.

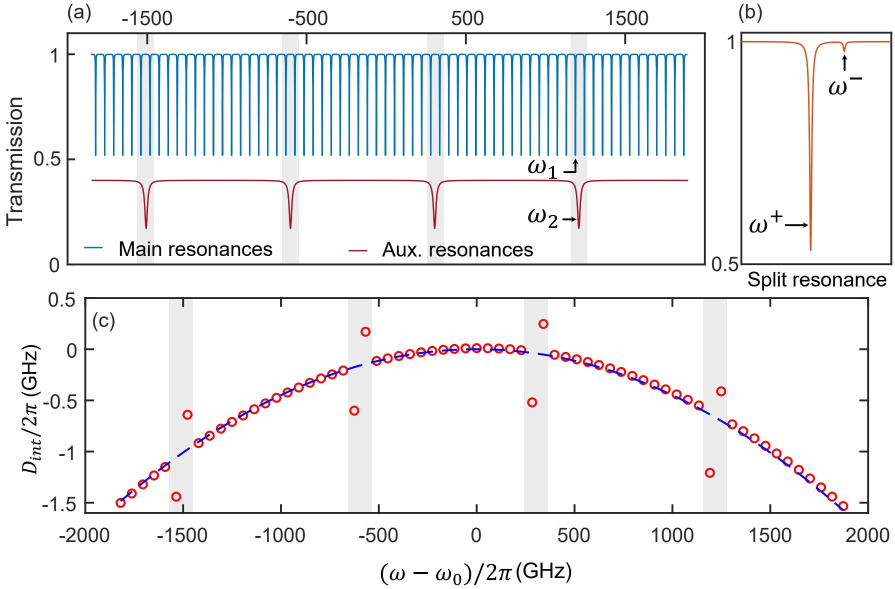

Figure 4.17: Illustration of the mode splitting and implication on the model dispersion of the coupled cavity system using parameters $a = 0.94, t_1 = 0.99, t_2 = 0.996, n_g = 2.1, R1\,(\text{main cavity}) = 400\,\mu\text{m}$, $R2\,(\text{auxiliary cavity}) = 25.1\,\mu\text{m}, \omega_0$ at 1550 nm, $\beta_1 = 6$ ps/km at 1565 nm, and $\beta_2 = 1000$ ps^2/km at 1565 nm. a) Transmission spectrum of the detached main and auxiliary cavity (offset by 0.5) according to equation 4.7. b) An avoided mode-crossing of uncoupled resonances at ω_1 and ω_2 according to equation 4.25. c) Integrated dispersion plot of the uncoupled main cavity (blue line) and coupled cavity (red circles).

We now investigate the integrated dispersion of linearly coupled cavities. First, we generate the resonance distribution of two cavities separately (Fig. 4.17(a)) using equation 4.7 according to the parameters given in Fig. 4.17. The mode interaction between the auxiliary and main cavities redistributes the resonance spectrum. Consequently, there is a split in the resonance frequencies. We consider the mode interaction of each auxiliary resonance with two adjacent main cavity resonances. Figure 4.17(b) shows the supermodes of the main resonance at ω_1 and auxiliary resonance at ω_2. The coupling rate between the auxiliary and main cavities is linked to the coupling coefficient κ according to $\kappa_{ex} = 2\kappa\sqrt{\mathrm{FSR}_1\mathrm{FSR}_2}$ [122]. As the auxiliary cavity FSR_1 is not an integer multiple of the main cavity FSR_2, the supermode spectra are not identical. The resonances are shifted dramatically from the uncoupled case at the coupling region. The integrated dispersion plot (red circle) in Fig. 4.17(c) elucidated the resonance shift at crossing points compared to the uncoupled main cavity (blue dashed line). The mode crossings can also be observed in a microresonator enabled by the vernier effect of the multimode resonances. We exploited this effect in paper [C] for the Q-factor management to achieve hyper-parametric oscillations vs bound states in the continuum.

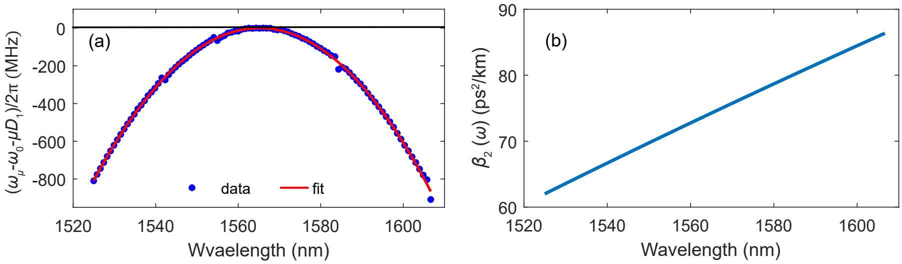

Figure 4.18: (a) Deviation of the resonance frequencies (D_{int}) from an equidistant frequency grid $\omega_0 + D_1\mu$ (gray line), where the reference mode is at 1565 nm. (b) Second-order dispersion plot of the microresonator.

Figure 4.18 illustrates an empirical dispersion calculation of a high-Q microresonator. The integrated dispersion (D_{int}) plot has the reference mode at 1565 nm and FSR $D_1/2\pi = 105.2$ GHz. There are weak mode crossing effects clearly visible at some resonance frequencies. The convex parabolic feature of the D_{int} plot suggests a normal dispersion of the microresonator. With 10 $\mathrm{ps}^2/\mathrm{km}$ accuracy in the β_2 calculation, one need $\sim 2\pi \times 90$ kHz resolution in the $D_2/2\pi$ for $D_1/2\pi = 2\pi \times 100$ GHz and radius 227 µm. In broadband spectroscopy, resolution accuracy in sub-mega hertz is impractical because of limited data points per trace of the oscilloscope and uncertainty in the laser calibration introduced by the RF detection unit. However, β_2 is measured with increased accuracy averaging $D_2/2\pi$ over a larger set of the resonances. The average extracted $D_2/2\pi \sim -730$ kHz corresponds to $\beta_2 = 73$ $\mathrm{ps}^2/\mathrm{km}$ at 1565 nm. It requires a separate polynomial fitting to estimate β_2 at a different resonance frequency. However, the GVD for all the resonance frequencies can be measured directly as in Fig. 4.18(b) from the equations 4.27 and 4.28.

Chapter 5

Microcombs dynamics

Microcombs are discrete frequency sources (lasers) that have unleashed enormous possibilities in frequency synthesis and metrology. The generation of microcomb is based on the Kerr nonlinear effect of four-wave mixing (FWM) processes. In particular, degenerate FWM processes generate a signal photon (ω_s) and an idler (ω_i) photon from two pump photons (ω_p). The conservation of energy ($2\omega_p = \omega_s + \omega_r$) ensures new equidistant frequency pairs. However, the coherence properties of microcombs were not known until Ferdous et al. demonstrated the microcomb phase measurement [136]. The phase measurement of the microcombs is crucial but challenging to implement. It provides physicists to investigate the comb dynamics, coherence of the spectrum, and ultra-short pulse in the cavity. In the following, we discuss the dynamics of field propagation in nonlinear media and the formation of soliton combs.

5.1 Optical field propagating in a nonlinear medium

The wave optics model governed by Maxwell's equations describes the field distribution in the waveguide. According to wave optics, waveguides support only finite eigenmodes with a specific wave vector [120]. In the propagation of the field, it is prominent to consider the Kerr effect (discovered by John Kerr in 1875) due to the nonlinear interaction of light. It represents an effect of intensity dependent refractive index (n) in the medium:

$$n = n_0 + n_2|E|^2, \tag{5.1}$$

where n_0 is a constant refractive index. The nonlinear-index coefficient n_2 is a function of susceptibility $\chi^{(3)}$. The typical value of n_2 is 2.4×10^{-17} m^2/W for Si_3N_4 [137]. The propagation of the field in a medium is modeled by the field envelope rather than the field itself. The evolution of the field envelope in a single-mode nonlinear medium is well described by the nonlinear Schrödinger equation (NLSE) according to [138]

$$\frac{\partial E}{\partial z} = \left(-\frac{1}{2}\alpha + i\sum_{n\geq 2}\frac{\beta_n}{n!}\left(i\frac{\partial}{\partial t}\right)^n + i\gamma|E|^2 \right) E, \tag{5.2}$$

where E is the slowly varying field envelope guided along the waveguide (z-axis). The propagation loss per unit length is α while β_n denotes the coefficients of the Taylor expansion of the propagation constant. The nonlinear parameter γ is a function of n_2 and the effective mode area. Nonlinear effects such as self-phase modulation (SPM), cross-phase modulation (XPM), and four-wave mixing (FWM) are governed by the γ parameter. This nonlinear differential equation is challenging to solve analytically. Therefore numerical simulations using the split-step Fourier method are widely adopted to emulate the nonlinear field propagation dynamics [138].

In a cavity, the field propagation dynamics consider the evolution of a slowly-varying field over consecutive round trips. It can be described in two sequential steps: applying the coupling equation and the field propagation for each round trip (known as the Ikeda map) [139]. In the cavity, the field evolves under the influence of propagation loss, dispersion, and Kerr nonlinearity according to equation 5.2. At a coupling region, there is an interference of the optical field described as

$$E^m(0,t) = \sqrt{\theta}E_{in} + \sqrt{1-\theta}E^{(m-1)}(L,t)e^{j\delta_0}, \tag{5.3}$$

with θ (equivalent to κ^2 in section 4.1.1) denoting the power coupling coefficient, E_{in} driving field, E^m m^{th} ($m \in \mathbb{N}$) roundtrip field, and L is the cavity length. The parameter δ_0 represents a relative phase shift of the wave compared to the phase of closest resonance ($\delta_0 = \Delta\omega/\text{FSR}$). This is often called the detuning parameter and is applied at the end of each roundtrip. The Ikeda map model is widely used to simulate the evolution of pulses in microresonators.

5.2 The Lugiato-Lefever equation and bistability

The Ikeda map is a model to simulate how the field evolves in the cavity. This model can be simplified into a single equation called the Lugiato-Lefever equation (LLE) [140]. The LLE provides an analytical understanding of the initialization and dynamics of microcombs. The derivation of the LLE assumes negligible field changes over a single roundtrip i.e. $E^{m-1}(L,t) = E^{m-1}(0,t) + L\frac{\partial E}{\partial z}$. With an approximation of a weak coupling and small detuning equation 5.3 turns out to be

$$E^m(0,t) \approx \sqrt{\theta}E_{in} + E^{(m-1)}(0,t)(1-\theta/2+i\delta_0) + L\frac{\partial E}{\partial z}. \qquad (5.4)$$

Applying the equations 5.4 and 5.2 on a slow time evolution of the wave $\frac{E^m(0,t)-E^{m-1}(0,t)}{t_r}$ over a roundtrip time (t_r) leads to the LLE equation

$$t_r\frac{\partial E}{\partial \tau} = \left[-\sigma - i\delta_0 + iL\sum_{n\geq 2}\frac{\beta_n}{n!}\left(i\frac{\partial}{\partial t}\right)^n + i\gamma L|E|^2\right]E + \sqrt{\theta}E_{in}, \quad (5.5)$$

where $\sigma = (\alpha L+\theta)/2$ denotes the total cavity losses in a single roundtrip and τ is the slow time. This equation describes the diverse non-linear dynamics of the cavities including but not limited to bistability [141], modulation instability [142], Kerr frequency combs [143]. The numerical simulation of the LLE enables the evaluation of the stable regions in the parameter space [144].

The LLE can describe the steady state behaviours of the microcombs driven by the CW field. All the time-dependent functions are dropped from the LLE to get the steady-state solution (below) of the field envelope circulating in the cavity.

$$(-\sigma - i\delta_0 + i\gamma L|E|^2)E = -\sqrt{\theta}E_{in}. \qquad (5.6)$$

This is a complex third-order polynomial equation in E. To simplify the solution, we multiply both sides with their conjugate:

$$\theta|E_{in}|^2 = (\sigma^2+\delta_0^2)P - 2\gamma L\delta_0 P^2 + \gamma^2L^2P^3, \qquad (5.7)$$

where $P = |E|^2$ is the intracavity power. Figure 5.1(a) shows the steady-state solutions as a function of the detuning parameter. The intracavity (resonance) power is symmetric in the linear regime as discussed in chapter 4 with the FWHM of 2σ. In the presence of a nonlinear phase shift, the resonance becomes tilted and has three possible solutions. Figure 5.1(b) also shows the intracavity power against the input power for various detuning values. It is worth noting that stable solutions are the minimum and maximum power of the bistability region. The unstable regions are indicated by the dashed lines [145].

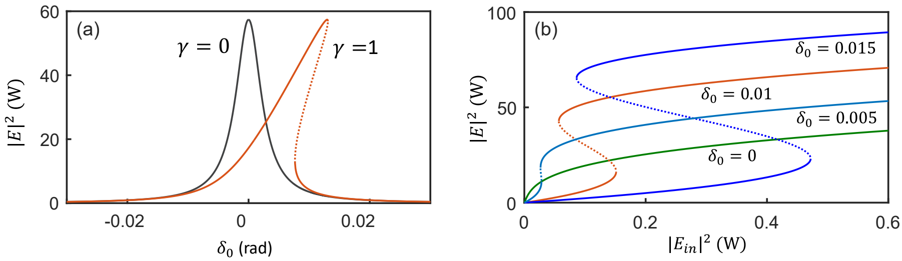

Figure 5.1: Bistability curves showing the intracavity power against a) detuning for $|E_{in}|^2 = 75$ mW and b) pump power for $\gamma = 1\text{W}^{-1}\text{m}^{-1}$ using parameters: $\alpha = 3$ dB/m, $\theta = 0.005$, $L = 226$ µm.

5.3 CW pump to microcomb generation

While the bistability analysis only considered the CW solution, the presence of perturbation (can be quantum fluctuation) excites modulation instability (MI). This is a form of parametric amplification that initializes the comb generation processes in the cavity from weak modulations on the CW pump. This state is highly unstable and grows exponentially [138]. From the LLE, a gain coefficient profile for MI can be derived by applying a small perturbation in the field envelope. The potential gain coefficient at a frequency offset $\Delta\omega$ from the pump is [146]:

$$g(\Delta\omega) = -\frac{\sigma}{t_r} + \frac{1}{t_r}\left((\gamma LP)^2 - \left(\delta_0 - 2\gamma LP - L\sum_{n\geq 2,\text{even}} \frac{\beta_n}{n!}\Delta\omega^n\right)^2\right)^{\frac{1}{2}}. \tag{5.8}$$

Figure 5.2 shows the MI gain along with the resonance spectrum neglecting the higher-order dispersion. The gain has to overcome both the propagation and coupling losses for the parametric amplification.

The gain spectra initialized by MI and pump experience cascaded four-wave mixing (FWM) processes leading to equidistant comb lines. The maximum MI gain at a certain $\Delta\omega$ satisfies $\Delta\omega^2 = 2(\delta_0 -$

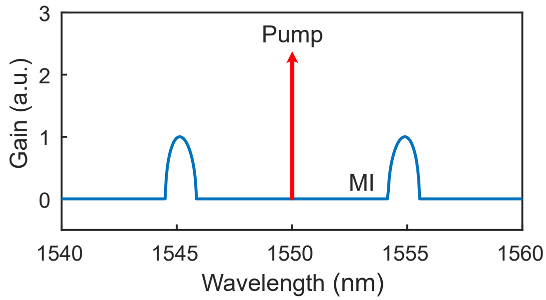

Figure 5.2: MI gain spectrum (blue) with the CW pump (red) plot using parameters: $\gamma = 2$ W^{-1}m^{-1}, $P = 100$ mW, $\beta_2 = -100$ ps^2/km, $\delta_0 = 0.005$ rad, $L = 150$ mm, $n_g = 2$.

$2\gamma LP)/(\beta_2 L)$ neglecting higher-order dispersion. This is a phase-matching condition for the MI gain. It suggests that the MI is accessible in the anomalous GVD ($\beta_2 < 0$) for $\delta_0 < 2\gamma LP$. This is a regime where the dissipative Kerr soliton (DKS) comb is generated. In paper D, we used a microresonator of anomalous GVD to generate dissipative single and multiple soliton combs. In the normal GVD regime($\beta_2 > 0$), MI requires $\delta_0 > 2\gamma LP$. However, the resonance detuning can be engineered and induce a localized anomalous GVD. This is enabled by the idea of mode coupling. In [128], the excitation of dark pulses (dark comb) was demonstrated with the aid of mode interactions in normal dispersion microresonators. In addition, linear coupled cavities implemented in [126,147] allow controlled mode interaction for DKSs generation in the normal dispersion region. In paper D, we used this concept to generate one of the DKSs to exemplify the characterization technique discussed in section 6.1.3.

DKS is described in anomalous dispersion as a double balance of losses with parametric gain and GVD with SPM [148]. This is generated by scanning the CW laser from the blue to the red side of the resonance. In general, the comb states pass through a chaotic region. The final comb state depends on the initial noise condition [143]. However, the chaotic states can be avoided by taking an advanced route in the parameter space [144]. The soliton states can be controlled by tuning the laser [149] or thermo-optic effect [150].

Figure 5.3(a) shows the evolution of the DKS dynamics in the microresonator using the Ikeda map model. The detuning of the laser towards the cavity resonance builds up the intracavity power and leads

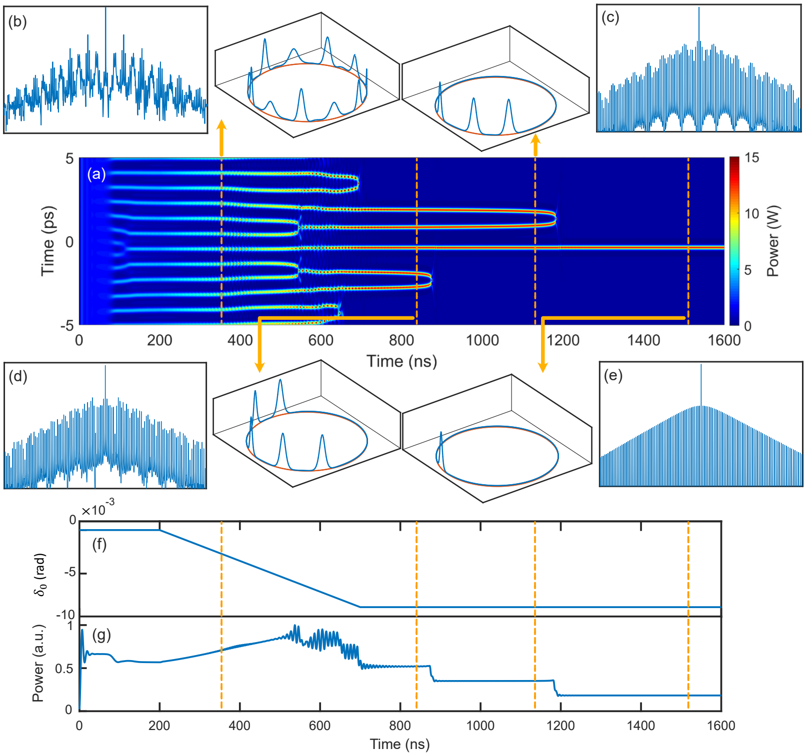

Figure 5.3: Dissipative Kerr soliton dynamics in the microresonator with the parameters: $\beta_2 = -150$ ps^2/km, $\gamma = 1.09$ W^{-1}m^{-1}, $n_g = 2.1$, FSR=100 GHz, $\theta = 0.00034$, $P_{in} = 60$ mW, $\alpha = 9$ dB/m. a) Evolution of the field power in the microresonator. b-e) Spectral response and temporal profile at the different instances of the comb evolution. f) Detuning of the pump from the nearest cold cavity resonance location. g) Intracavity power versus time.

to MI and chaotic states. The CW steady-state resolves at a certain detuning into bistability generating multiple DKSs in the cavity. The spectral and temporal profiles at various regimes of the comb dynamics are shown in Fig. 5.3(b)-(e). Figure 5.3(f) and (g) demonstrate the detuning of the pump from the cold cavity resonance and the evolution of intracavity power respectively.

5.4 DKS characteristics

One analytical steady state solution of the LLE for a non-dissipative medium turns out to be a soliton pulse $A_s(t)$ [57].

$$A_s(t) = \sqrt{\frac{2\delta_0}{\gamma L}}\mathrm{sech}\left(t\sqrt{\frac{2\delta_0}{\mid \beta_2 \mid L}}\right). \tag{5.9}$$

Instead of a CW pump, this non-dissipative soliton can be used as a source to simulate the DKS. In microresonators, the DKS pulse circulates on top of a CW background. The background is defined by the lower level of the CW bistability. We add this complex background to the non-dissipative soliton pulse and use it as a driving pulse in the Ikeda map simulation of the DKS in the microresonator. The temporal intensity and phase profile of the driving pulse is shown in Fig 5.4.

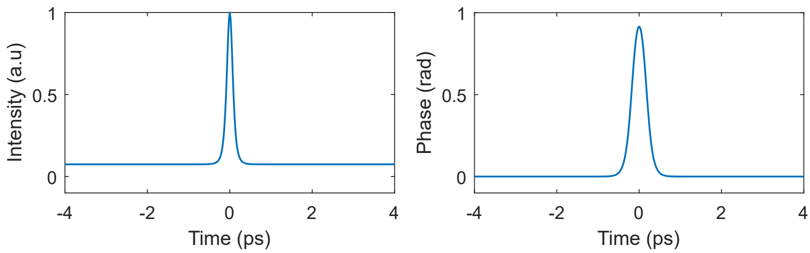

Figure 5.4: Temporal soliton pulse (a) and phase profile (b). The parameters are as follows: $\beta_2 = -65$ ps^2/km, $\delta_0 = 0.028$ rad, $\gamma = 1$ W^{-1}m^{-1}, $n_g = 2.1$, FSR=100 GHz, $\theta = 0.0014$, $\alpha = 3$ dB/m, $P_{\text{in}} = 20$ dBm.

Figure 5.5 is the Ikeda map simulation of the single DKS and multi-DKS (two solitons) for a 100 GHz repetition rate. The multi-DKS has a spectral modulation of a 10-FSR period.

The DKS microcombs in both temporal and spectral intensity responses are hyperbolic secant. Figure 5.6 is the waveform of the single DKS. The temporal intracavity intensity and phase profiles are in Fig. 5.6(a) and (b). The phase response of the DKS spectrum is approximately constant except at the pump frequency (Fig. 5.6(c)). This pump phase offset is attributed to the field interaction at the coupling region [151] and self-organization in the comb formation process [152]. The differential phase of the spectrum is shown in Fig. 5.6(d). In paper D (E), we illustrated the stepped (multi) heterodyne technique to reconstruct the differential phase of the single (coupled) cavity DKS combs.

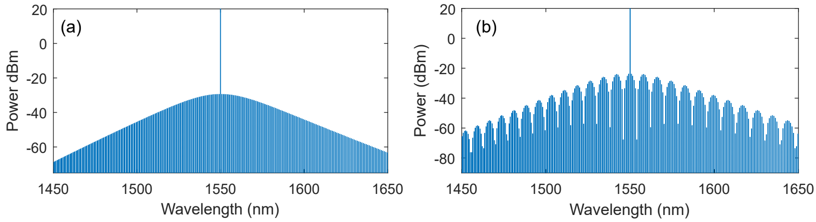

Figure 5.5: Simulated 100 GHz single (a) and multisoliton (b) combs. The comb parameters are as follows: $\alpha = 3$ dB/m, $\beta_2 = -65$ ps^2/km, FSR = 100 GHz, $n_g = 2.1$, $\gamma = 1$ W^{-1}m^{-1}, $\delta_0 = 0.028$ rad, $P_{\text{in}} = 20$ dBm, $\theta = 0.0014$.

The spectral phase profile enables inferring a temporal pulse in the cavity which otherwise is challenging to measure (detailed in chapter 6 and paper D).

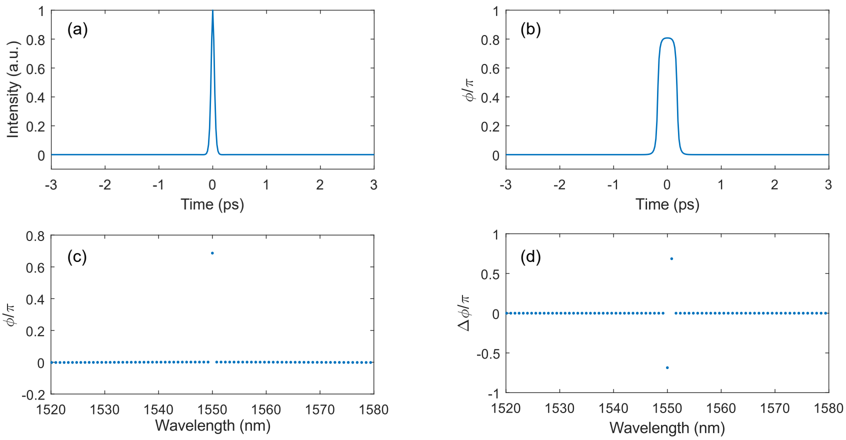

Figure 5.6: Temporal and spectral waveform of the single DKS simulated by the Ikeda map in Fig 5.5(a). (a) Temporal pulse profile. (b) Temporal phase profile. (c) spectral phase of the 100 GHz repetition rate comb modes. (d) Differential phase of the comb modes.

Figure 5.7 shows the waveform of the multi-DKS comb. It has two intracavity soliton pulses circulating in the cavity at 1 ps apart. The temporal intensity and phase profiles are shown in Fig 5.7(a) and (b). The phase profile (Fig. 5.7(c) and (d)) shows a π phase transition at the spectral intensity modulation dip. In paper D, we have elucidated the heterodyne method of capturing such a phase distribution and reconstruction of the pulse profile.

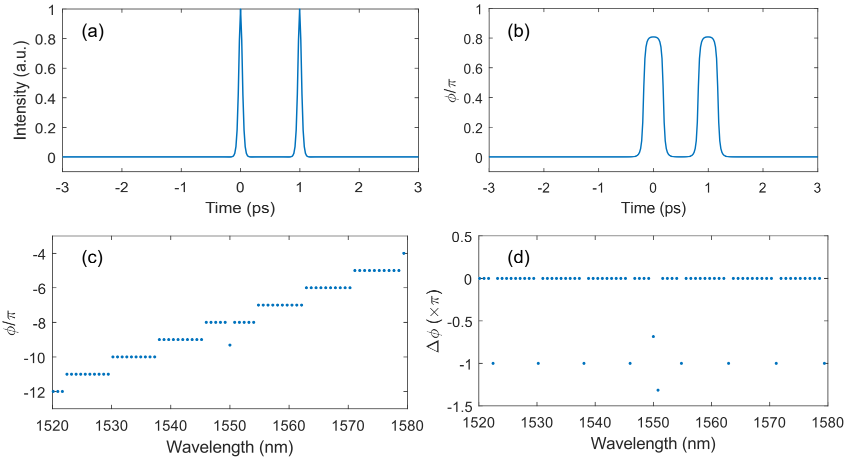

Figure 5.7: Temporal and spectral waveform of the multi-DKS simulated by the Ikeda map in Fig 5.5(b). (a) Temporal pulse profile. (b) Temporal phase profile. (c) Spectral phase of the 100 GHz repetition rate comb modes. (d) Differential phase of the comb modes.

Chapter 6

Linear pulse characterization techniques

6.1 Characterization of frequency combs

The rapid development of ultrafast optics in the past decades has found a myriad of applications. The manipulation of the amplitude and phase of individual spectral lines using a pulse shaper enables the generation of an optical arbitrary waveform (OAW) [62, 153]. To completely describe an optical pulse requires either spectral or temporal amplitude and phase profile of the electric field. There has been a significant effort expended toward the development of pulse characterization techniques. Broadly, these techniques are categorized into linear and nonlinear characterization methods. Methods based on optical nonlinearities have been reported such as frequency-resolved optical grating (FROG) [154] and spectral phase interferometry (SPIDER) [155]. In addition, the autocorrelation technique is also widely adopted for estimating the pulse duration [156]. These nonlinear techniques typically apply to measure low-duty-cycle pulses, which require high peak power to generate a second harmonic signal.

However, the linear method can be applied to arbitrary waveforms for complete amplitude and phase characterization of optical pulses. These techniques focus on phase and amplitude spectral characterization and recreate its temporal intensity and phase profile. The basic idea is to measure the phase difference between modes. The direct optical spectral phase measurement (DOSPM) [157] measures the phase difference between modes selected by narrow slits (filters). It is based on the cross-correlation between a transfer-limited pulse and the interference of the modes. In [153, 158], the phase difference is inferred from the measured beat note between adjacent spectral modes. However, measuring such a pulse requires a detector that can respond faster compared to the pulse width. The state-of-the-art detection unit hardly reaches 100 GHz analog bandwidth.

As a complex spectrum analyzer, an optical heterodyne technique of beating a reference laser with the spectral modes is illustrated in [159, 160]. This translates the phase difference between the adjacent optical modes to the phase of an electrical signal at an arbitrarily low frequency. In [161], a reference laser is phase-modulated to record a beat note with a low bandwidth receiver. Given the requirement of a series of measurements, these techniques are limited by the measurement speed. An electric-field cross-correlation dual-comb technique is introduced for optical arbitrary waveform characterization in [162]. It provides both fast data acquisition and higher sensitivity but needs pre-calibration of the reference comb.

In the realm of microcombs, an intensity autocorrelation is commonly used to measure the phase of the comb lines [61, 136]. In this technique, the relative phase of comb lines is iterated via a spatial light modulator (pulse shaper) to obtain a maximum amplitude modulation in the autocorrelation response. This is the idea of optimizing the spectral phase of a pulse until the shortest (transform-limited) pulse is realized. Then the phase of the comb lines is inferred from the reverse of the phase applied to the pulse shaper. In [57], a conventional pulse characterization technique frequency-resolved optical grating (FROG) was implemented to demonstrate transform-limited optical pulses of a single-soliton 35 GHz comb. For an integrated platform, it is challenging to implement FROG due to the high repetition rate and the fact that the pulse waveforms of the microcombs have very low energy. In addition, there are plenty of microcombs that are not transform-limited, hence further reducing the peak intensity, such as, e.g., dark combs [128], and coupled cavity combs [126, 163], and soliton crystals [164]. However, the intensity autocorrelation technique allows measuring phases of the low-power comb lines and offers a high dynamic range. This technique was adopted to fully characterize distinct microcombs states in [61, 128]. The autocorrelation measurement is a nonlinear process requiring a high signal power to induce sufficient second harmonic yield. Therefore, it needs an optical amplifier to boost the signal power. However, the gain bandwidth of the amplifier or the bandwidth of the pulse shaper, therefore, limits the measurement range. In addition, this method is time-consuming due to the line-by-line phase iteration of the comb modes. In [165], a concept of electric field cross-correlation in the microcomb phase measurement is reported. In this method, a calibrated reference comb is heterodyned with the comb under test. It shares the same technical principle as dual-comb spectroscopy, allowing reconstruction of the phase in a single-shot measurement. Nonetheless, the necessity of reference comb phase calibration ultimately leads to the aforementioned limitations i.e. limited bandwidth of the optical instrumentation. In what follows, we discuss the linear heterodyne phase difference measurement techniques used in papers [D, E] that overcome these limitations.

6.1.1 Stepped heterodyne characterization

Stepped heterodyne is a linear method of complex spectral and temporal measurement of periodic optical signals. The idea lies in beating the signal waveform with a continuous-wave laser. The laser is tuned across the comb tones in a stepped-wise manner with a step size equal to the repetition rate of the comb as shown in Fig. 6.1(a). The phase of the consecutive lines is embedded in the downconverted radio-frequency beat notes. The stepped heterodyne technique described does not require reference laser calibration. It measures the differential phase comparing the phase of photodetected beatnotes which is independent of the phase noise of the seed laser and reference laser. The beatnotes power is proportional to the product of the reference laser and comb line power. This in turn provides high sensitivity. This technique has been implemented to characterize various periodic signals. In [159], optical pulses and passively mode-locked lasers were characterized for both amplitude and phase in the spectral and temporal domains. An electronic down conversion with the aid of a local oscillator of the detected beatnotes allows characterizing a $\sim$ 40 GHz modelocked laser [166].

For an optical frequency $\omega_{s(ref)}$, phase noise $\phi_{s(ref)}$, and power of the optical carrier $P_{\mu(ref)}$ (reference signal), the complex electric field of the periodic signal under test of period $2\pi/\omega_r$ can be written as:

$$E_{\mathrm{CUT}}(t) = \sum_{\mu=-n}^{n} (\sqrt{P_\mu}\exp(j\mu\omega_r t + j\phi_\mu)\exp(j\omega_s t + j\phi_s(t)). \tag{6.1}$$

The complex electric field of the reference signal is:

$$E_{ref}(t) = \sqrt{P_{ref}}\exp(j\omega_{ref}t + j\phi_{ref}(t)). \tag{6.2}$$

The crucial parameter under investigation is the static spectral phase ϕ_μ of the μ^{th} mode number. In the stepped heterodyne technique these two signals are mixed on a square law balanced photodetector. Figure 6.1(c) is the interference pattern acquired from the real-time scope for 200 ns of interval. This in turn generates three nontrivial RF heterodyne beat tones (Fig. 6.1(d)).

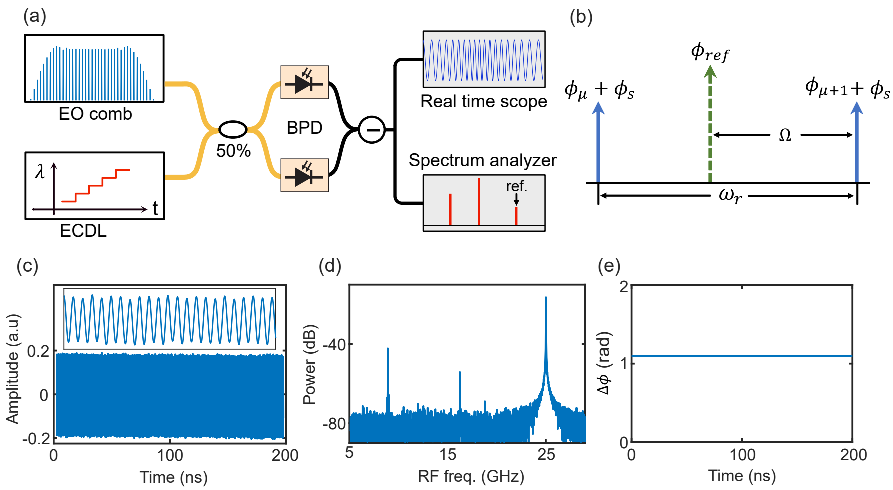

Figure 6.1: Stepped heterodyne optical complex spectrum analyzer.(a) Schematic diagram showing the beating between the EO-comb and reference laser (ECDL). (b) Spectral lines with the corresponding phase. (c) Interference pattern of beat signals and zoom in the inset. (d) RF beat note spectrum. (e) Differential phase of the one pair of the EO-comb lines. ECDL: External cavity diode laser, BPF: Balanced photodiode.

Consider the reference laser is in between comb modes μ and $\mu + 1$ as shown in Fig. 6.1(b). The complex electric field of RF beat tones can be expressed as [159]

$$\begin{aligned} E_{beat}(t) = &\sqrt{P_{ref}P_{\mu+1}}\exp(j(\Omega t + \phi_{ref}(t) - \phi_s(t) - \phi_{\mu+1})) \\ &+ \sqrt{P_{ref}P_\mu}\exp(j((\omega_r - \Omega)t - \phi_{ref}(t) + \phi_s(t) + \phi_\mu)) \\ &+ \sqrt{P_{net}}\exp(j(\omega_r t + \phi_{net})), \end{aligned} \tag{6.3}$$

with $\Omega \leq \omega_r/2$ denoting detuning of the reference laser from the nearest mode. P_{net} and ϕ_{net} denote accumulate power and phase of beating between adjacent comb modes respectively. The bandwidth limit of the detector is assumed to be equal to the repetition rate of the comb f_r. The first two terms correspond to the beating of the reference signal with the two nearest comb lines. The beating of adjacent comb lines corresponds to the last term. This beating signal is common for all stepped measurements and independent of the location of the reference laser. Therefore, this signal is used as a reference in the phase difference calculation. These spectra are retrieved by applying Fourier transform and digital filters centered at Ω, $\omega_r - \Omega$, and ω_r. The combination of the first two terms results in $P_{ref}\sqrt{P_\mu P_{\mu+1}}\exp(j(\omega_r t + \phi_\mu - \phi_{\mu+1}))$ with no phase noise contributions. The product of this signal with the conjugate of the reference signal yields a signal with an argument $\phi_{\mu-1} - \phi_\mu - \phi_{net}$ as a function of time Fig. 6.1(e). The differential phase $\Delta\phi_\mu = \langle\phi_{\mu-1} - \phi_\mu - \phi_{net}\rangle$ is then calculated by taking the average of this signal. The constant phase offset term ϕ_{net} introduces a linear phase in the spectral phase reconstruction. While it shifts the pulse in time, it will not affect in the reconstruction of the pulse shape. Figure 6.2 shows the stepped heterodyne technique applied to an EO comb and validated with the simulation. The EO-comb consists of cascaded modulators in a sequence as PM-PM-IM.

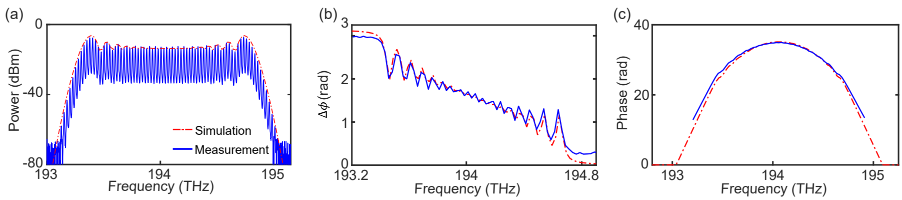

Figure 6.2: Stepped heterodyne complex spectrum analysis of the EO comb (red: simulation and blue: measurement). (a) EO comb spectrum. The modulation depth was set to 14.25 in the simulation. (b) Differential phase profile. (c) Reconstruction of the spectral phase response.

6.1.2 Multi-heterodyne characterization

Multi-heterodyne pulse characterization technique shares a similar principle as dual-comb spectroscopy [162, 167]. This technique is implemented to measure the complex spectrum and reconstruct the dynamic pulse trains [168]. The multi-heterodyne enables the recording of the complex spectrum of the comb under test (CUT) in a single trace. Instead of stepping CW laser between comb lines, this method uses another comb of different repetition rates as a reference signal. We reported this technique in the context of microcomb in Paper [E]. The offset in the repetition rate leads to the temporal scanning of the comb pulses. The coherent detection results in the cross-correlation of the two combs field envelope. This yields multiple discrete heterodyne beat notes or RF combs containing information on the amplitude and phase of each line in the CUT. The phase of CUT lines is retrieved by comparing the phase of RF combs. In what follows, we describe the multi-heterodyne spectroscopy using two EO combs.

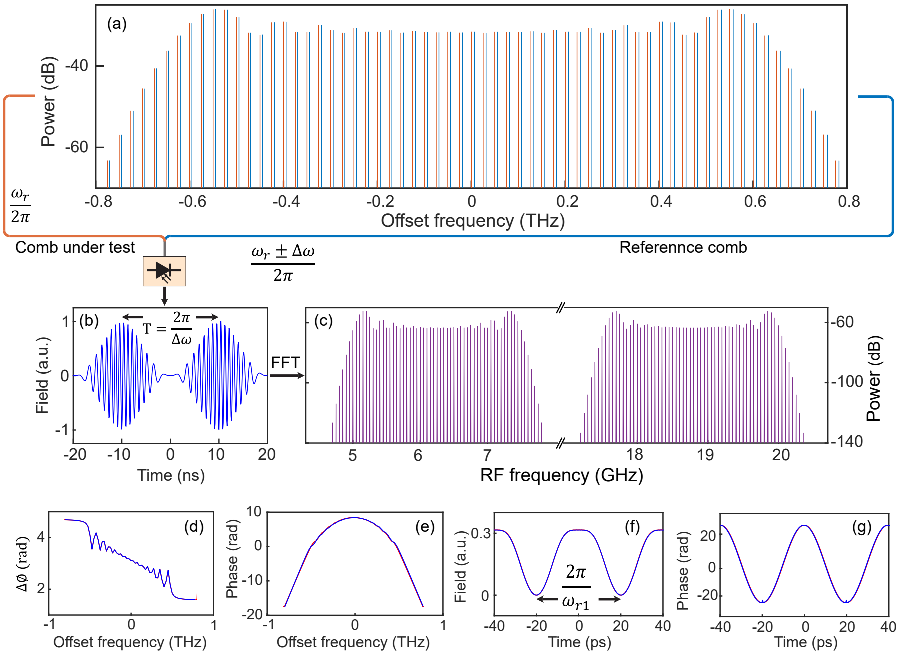

Figure 6.3: Simulation of multiheterodyne spectroscopy. (a) EO combs with a 50 MHz difference in the repetition rate (red: 25 GHz CUT and blue: 25.05 GHz reference comb).(b) Interferogram of period 20 ns. (c) Radio frequency spectrum of two detuned combs. Features of the CUT (red: actual and blue: recovered): (d) Differential phase spectrum, (e) spectral phase profile, (f) pulse profile, and (g) temporal phase profile.

As the CUT field in equation 6.1, we define the reference comb field according to:

$$E_{\text{ref.}}(t) = \sum_{\mu=-n}^{n} (\sqrt{P_{\text{ref.}\mu}}\exp(j\mu(\omega_r \pm \Delta\omega)t + j\psi_\mu)\exp(j(\omega_{\text{ref.}}t + j\phi_{\text{ref.}}(t)). \tag{6.4}$$

The parameters have a similar meaning to the variables in the CUT field equation. The reference comb pulse steps across the entire CUT pulse periodically in every $2\pi/\Delta\omega$ second or after $\omega_r/\Delta\omega$ CUT pulses. In our simulations, we set the combs spacing difference $\Delta\omega/2\pi = 50$ MHz and $\omega_r/2\pi = 25$ GHz. The driving source frequency ($\omega_{\text{ref.}}$) was set to $\omega_s + \omega_r/4$ (Fig. 6.3(a)). This ensures the detection of the maximum number of RF comb lines without spectrum folding. The coherent heterodyne detection generates an interferogram (Fig. 6.3(b)) of period $2\pi/\Delta\omega$. Fourier transform of the interferogram generates sets of RF combs. The two adjacent sets of RF combs as shown in Fig. 6.3(c)) can fully characterize the CUT. The idea is to pair up the RF comb lines one from each set that corresponds to the adjacent CUT lines. Then the (differential) phase profile of the CUT (Fig. 6.3(d)-(e)) is merely calculated by applying the technique discussed in section 6.1.1. The temporal profiles in Fig 6.3(f) and (g) are inferred from the complex optical spectrum using the envelope function of equation 6.1.

6.1.3 Microcomb characterization

Stable microcombs can be generated in numerous forms. The microcombs can have various coherent states and complex pulse profiles [47]. It is important to measure the phase of comb lines to understand the comb dynamics and perform a full-field characterization. However, measuring the phase for broadband range encounters several challenges in the context of microcombs. In addition, repetition rates can go beyond the state-of-the-art electronics detection range. In paper [D], we implemented the stepped heterodyne technique in the realm of microcombs. The large repetition rate was made accessible by the electro-optic downconversion of the comb lines. For this, we used a phase modulator (PM) to bring the comb lines closer in the form of sidebands. The sideband carries the phase information of the comb line with an irrelevant constant offset. It is also possible to acquire the complex spectrum of a comb in a single real-time trace by using a reference comb of slightly different repetition rate [168–170]. Paper [E] illustrates the multi-heterodyne technique by using coupled cavity microcombs driven by two free-running lasers. These methods provide internal phase reference and excellent dynamic range.

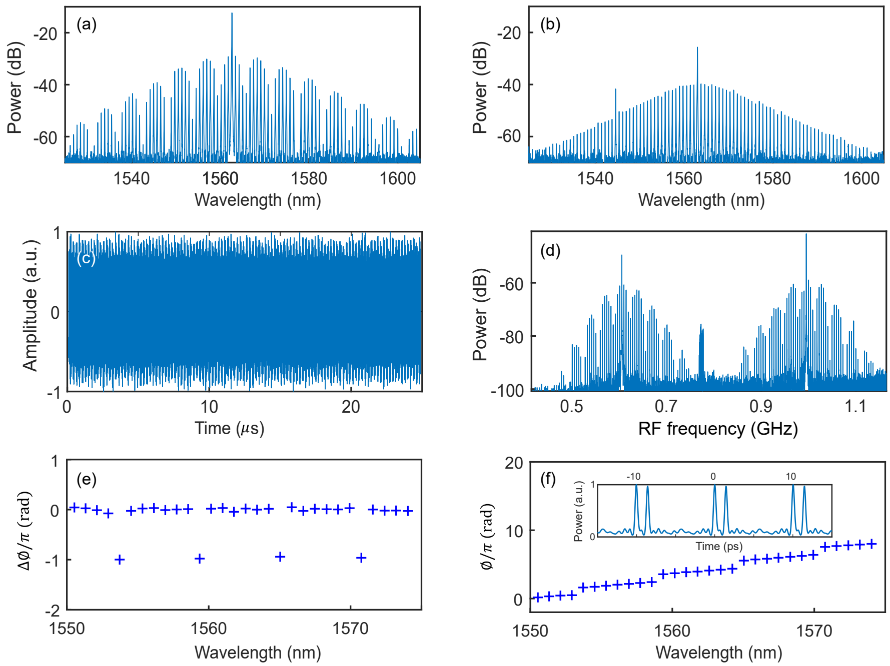

Figure 6.4: Multi-heterodyne spectroscopy of the coupled cavity soliton comb. (a) Multisoliton CUT with pump at 1562.65 nm. (b) Single soliton reference comb with pump at 1563.2 nm. (c) Interferogram recorded for 25 µs of period 0.2 µs. (d) RF comb spectrum after Fourier transform of the interferogram. (e) Differential phase showing π periodic phase discontinuities. (f) Phase of the comb lines (Inset: reconstructed pulse profile.)

Here, we provide a further illustration of the technique characterizing a multi-soliton comb in a coupled cavity resonator. In Fig. 6.4, we used a reference single soliton microcomb (Fig. 6.4(b)) of a slightly different repetition rate $\Delta\omega/2\pi \sim 5$ MHz instead of a stepped tunable laser. The intensity modulator of the CUT (Fig. 6.4(a)) gives access to the pair of comb lines and generates an RF reference signal. Figure. 6.4(c) is an interferogram recorded for 25 µs duration and corresponding RF combs in Fig. 6.4(d). The interferogram has a period of ~200 ns. The combs are driven by separate free-running lasers. By locking the lasers to the stable optical reference system (ORS), we can average the interferogram over a longer duration and achieve a higher sensitivity. We calculated the differential phase of the multi-soliton comb in Fig. 6.4(e) and phase profile in Fig. 6.4(f) as discussed in section 6.1.2. The 7-FSR modulation in the comb envelope indicates two pulses in the cavity of ∼1.45 ps apart as shown in the inset. This technique has the potential in tracing the soliton dynamics [171] by dividing the measured interferogram into the segments that belong to the particular comb states.

Chapter 7

Future outlook

This thesis has focused on the interferometric modality of characterizing photonic devices. The tuning laser that probes the sample was calibrated with a self-referenced frequency comb. It enabled ultra-wide bandwidth and a large dynamic measurement range of an SWI system. The soliton dynamics in a microcavity with temporal and spectral distributions were illustrated. There are numerous fascinating follow-up research questions related to the work presented in this thesis. Here, I highlight some areas that in my opinion are worth to be explored.

- Papers A-B illustrated the fiber laser self-referenced comb calibrated swept-wavelength interferometry. The equidistant frequency lines from the comb provide thousands of precise references in laser calibration. It would be interesting to replace the fiber comb with the microcomb. Microcombs of $<$ 20 GHz can be generated and the gap can be filled by generating subcombs with an electro-optic modulation. The RF frequency can be set such that spacing between the lines is even throughout the spectral range.

- Paper D demonstrated the stepped heterodyne technique to reconstruct the differential phase of the microcombs. This involves stepping the laser with the repetition rate of the comb. In Paper E, the tuning laser is replaced with another microcomb of a slightly different repetition rate. This enables the spectroscopy of a CUT from a single-shot interferogram trace. It would be interesting to trace the interferogram while the CUT is in a transition phase from the MI to comb states. This allows imaging of comb dynamics in the cavity.

- In the framework of the Innovative Training Network (ITN) called MICROCOMB, I had a unique opportunity to actively collaborate with world-leading partners in the field. During my secondment at the Max Plank Institute for the Science of Light and Menlo Systems in Germany, I learned a dual-pumping technique and locking to the self-reference frequency comb. It is worth exploring the injection locking of the pumps to the comb lines at the onset of the microcomb. This would enable not only the coherent broadening of the microcomb but purity transfer of the self-reference frequency comb to the microcomb lines.

Chapter 8

Summary of papers

Paper A

Frequency-comb-calibrated swept-wavelength interferometry,
Optics Express, 29, 15, 24363-24372, 2021.

Here, we demonstrate the non-destructive broadband characterization in amplitude and phase of ultra-low-loss microresonators and spiral waveguides. The device under test is arranged in an interferometric configuration. The swept laser is calibrated using a self-referenced fiber laser comb to map the time axis of the acquired interference pattern into the frequency axis. The measured phase distribution of the resonances enables distinguishing intrinsic loss from coupling loss. The parametric fitting of the resonances is done based on the coupled mode theory.

My contributions: I conducted the measurements and simulations, and I wrote the paper with support from co-authors. I presented the work at CLEO EU 2021.

Paper B

Spectral interferometry with frequency combs,
Micromachines, 13, 4, 614, 2022.

In this work, we review the state of the art in linear interferometric techniques using a laser frequency comb source. We present different techniques; Fourier-transform spectroscopy, linear spectral interferometry, and swept wavelength interferometry, and highlight some applications.

My contributions: I wrote sections 4.3, 4.4, 5.3, and 5.4 in the manuscript.

Paper C

Hyperparametric oscillation via bound states in the continuum, *Physical Review Letters*, 130, 9, 09381, 2023.

In this work, we demonstrated the generation of high-power and efficient continuous waves in a Kerr nonlinear medium. This was enabled by bound states in the continuum in multi-mode microresonators via the dissipative coupling between resonance modes.

My contributions: I carried out the microresonator characterization using the SWI and helped in writing the manuscript.

Paper D

Differential phase reconstruction of microcombs, *Optics Letters*, 47, 13, 3351-3354, 2022.

In this paper, we show a linear heterodyne technique to characterize the single and coupled cavity microcombs. This technique enables measuring broadband differential phase between consecutive comb lines with unprecedented bandwidth and power sensitivity. The phase difference measurement of a high repetition rate comb is assisted by electro-optic downconversion.

My contributions: I conducted lab experiments and simulations with co-authors. I wrote the manuscript with co-authors and I presented the preliminary results at CLEO 2022.

Paper E

Multi-heterodyne differential phase measurement of microcombs, *submitted to Conference on Lasers and Electro-Optics Europe, 2023*

In this paper, we show a multi-heterodyne technique to characterize a coupled cavity microcomb. This technique enables measuring broadband differential phase between consecutive comb lines from a single-shot interferogram trace. The phase difference measurement of a high repetition rate comb is assisted by electro-optic downconversion.

My contributions: I conceived the idea and conducted lab experiments. I wrote the manuscript with co-authors.

References

[1] R. Soref and B. Bennett, "Electrooptical effects in silicon," *IEEE journal of quantum electronics*, vol. 23, no. 1, pp. 123–129, 1987.

[2] A. A. Jørgensen, D. Kong, M. R. Henriksen, F. Klejs, Z. Ye, Ó. B. Helgason, H. E. Hansen, H. Hu, M. Yankov, S. Forchhammer, P. Andrekson, A. Larsson, M. Karlsson, J. Schröder, Y. Sasaki, K. Aikawa, J. W. Thomsen, T. Morioka, M. Galili, V. Torres-Company, and L. K. Oxenløwe, "Petabit-per-second data transmission using a chip-scale microcomb ring resonator source," *Nat. Photonics*, no. 16, pp. 798–802, 2022.

[3] J. Lasky, S. Stiffler, F. White, and J. Abernathey, "Silicon-on-insulator (SOI) by bonding and ETCH-back," in *1985 International Electron Devices Meeting*, 1985, pp. 684–687.

[4] B. Mozumder, "Development of bonding and etchback silicon on insulator wafers," in *Journal of the Microelectronic Engineering Conference*, vol. 6, no. 1, 1996, p. 8.

[5] M. Bruel, "Process for the production of thin semiconductor material films," US Patent 5,374,564, 1994.

[6] M. Bruel and B. A. Auberton-Hervé, "Smart-cut: a new silicon on insulator material technology based on hydrogen implantation and wafer bonding," *Japanese journal of applied physics*, vol. 36, no. 3S, p. 1636, 1997.

[7] R. Soref and J. Larenzo, "All-silicon active and passive guided-wave components for λ= 1.3 and 1.6 µm," *IEEE J. Quantum Electron.*, vol. 22, no. 6, pp. 873–879, 1986.

[8] A. Rickman, G. Reed, and F. Namavar, “Silicon-on-insulator optical rib waveguide loss and mode characteristics,” *J. Lightwave Technol.*, vol. 12, no. 10, pp. 1771–1776, 1994.

[9] P. Dumon, W. Bogaerts, V. Wiaux, J. Wouters, S. Beckx, J. Van Campenhout, D. Taillaert, B. Luyssaert, P. Bienstman, D. Van Thourhout, and R. Baets, “Low-loss SOI photonic wires and ring resonators fabricated with deep UV lithography,” *IEEE Photonics Technology Letters*, vol. 16, no. 5, pp. 1328–1330, 2004.

[10] V. R. Almeida, R. R. Panepucci, and M. Lipson, “Nanotaper for compact mode conversion,” *Opt. Lett.*, vol. 28, no. 15, pp. 1302–1304, 2003.

[11] D. Taillaert, P. Bienstman, and R. Baets, “Compact efficient broadband grating coupler for silicon-on-insulator waveguides,” *Opt. Lett.*, vol. 29, no. 23, pp. 2749–2751, 2004.

[12] W. Bogaerts, R. Baets, P. Dumon, V. Wiaux, S. Beckx, D. Taillaert, B. Luyssaert, J. Van Campenhout, P. Bienstman, and D. Van Thourhout, “Nanophotonic waveguides in silicon-on-insulator fabricated with CMOS technology,” *J. Lightwave Technol.*, vol. 23, no. 1, p. 401, 2005.

[13] T. Komljenovic, D. Huang, P. Pintus, M. A. Tran, M. L. Davenport, and J. E. Bowers, “Photonic integrated circuits using heterogeneous integration on silicon,” *Proceedings of the IEEE*, vol. 106, no. 12, pp. 2246–2257, 2018.

[14] D. Huang, M. A. Tran, J. Guo, J. Peters, T. Komljenovic, A. Malik, P. A. Morton, and J. E. Bowers, “High-power sub-kHz linewidth lasers fully integrated on silicon,” *Optica*, vol. 6, no. 6, pp. 745–752, 2019.

[15] H. Park, A. W. Fang, O. Cohen, R. Jones, M. J. Paniccia, and J. E. Bowers, “A hybrid AlGaInAs-silicon evanescent amplifier,” *IEEE Photon. Technol. Lett.*, vol. 19, no. 4, pp. 230–232, 2007.

[16] C. Wang, M. Zhang, X. Chen, M. Bertrand, A. Shams-Ansari, S. Chandrasekhar, P. Winzer, and M. Lončar, “Integrated lithium niobate electro-optic modulators operating at CMOS-compatible voltages,” *Nature*, vol. 562, no. 7725, pp. 101–104, 2018.

[17] A. W. Fang, H. Park, O. Cohen, R. Jones, M. J. Paniccia, and J. E. Bowers, "Electrically pumped hybrid algainas-silicon evanescent laser," *Opt. Express*, vol. 14, no. 20, pp. 9203–9210, 2006.

[18] Q. Xu, B. Schmidt, S. Pradhan, and M. Lipson, "Micrometre-scale silicon electro-optic modulator," *Nature*, vol. 435, no. 7040, pp. 325–327, 2005.

[19] K. Greene, *Silicon photonics comes to market.* MIT Technol. Rev., Cambridge, MA, USA, Tech. Rep. 408520, Aug. 2007, https://www.technologyreview.com/2007/08/16/224040/silicon-photonics-comes-to-market/.

[20] A. Rahim, T. Spuesens, R. Baets, and W. Bogaerts, "Open-access silicon photonics: current status and emerging initiatives," *Proceedings of the IEEE*, vol. 106, no. 12, pp. 2313–2330, 2018.

[21] D. J. Blumenthal, R. Heideman, D. Geuzebroek, A. Leinse, and C. Roeloffzen, "Silicon nitride in silicon photonics," *Proceedings of the IEEE*, vol. 106, no. 12, pp. 2209–2231, 2018.

[22] J. Cardenas, C. B. Poitras, J. T. Robinson, K. Preston, L. Chen, and M. Lipson, "Low loss etchless silicon photonic waveguides," *Opt. Express*, vol. 17, no. 6, pp. 4752–4757, 2009.

[23] J. Boyd, R. Wu, D. Zelmon, A. Naumaan, H. Timlin, and H. Jackson, "Planar and channel optical waveguides utilizing silicon technology," in *Integrated Optical Circuit Engineering I*, vol. 517. International Society for Optics and Photonics, 1985, pp. 100–105.

[24] C. H. Henry, R. F. Kazarinov, H. J. Lee, K. J. Orlowsky, and L. Katz, "Low loss Si_3N_4-SiO_2 optical waveguides on Si," *Appl. Optics*, vol. 26, no. 13, pp. 2621–2624, 1987.

[25] J. S. Levy, A. Gondarenko, M. A. Foster, A. C. Turner-Foster, A. L. Gaeta, and M. Lipson, "CMOS-compatible multiple-wavelength oscillator for on-chip optical interconnects," *Nat. Photonics*, vol. 4, no. 1, pp. 37–40, 2010.

[26] W. D. Sacher, J. C. Mikkelsen, Y. Huang, J. C. C. Mak, Z. Yong, X. Luo, Y. Li, P. Dumais, J. Jiang, D. Goodwill, P. G.-Q. Lo, and

J. K. S. Poon, “Monolithically integrated multilayer silicon nitride-on-silicon waveguide platforms for 3-D photonic circuits and devices,” *Proceedings of the IEEE*, vol. 106, no. 12, pp. 2232–2245, 2018.

[27] D. Melati, A. Alippi, and A. Melloni, “Waveguide-based technique for wafer-level measurement of phase and group effective refractive indices,” *J. Lightwave Technol.*, vol. 34, no. 4, pp. 1293–1299, 2015.

[28] F. Morichetti, A. Canciamilla, C. Ferrari, M. Torregiani, A. Melloni, and M. Martinelli, “Roughness induced backscattering in optical silicon waveguides,” *Phys. Rev. Lett.*, vol. 104, no. 3, p. 033902, 2010.

[29] P. Del’Haye, O. Arcizet, M. L. Gorodetsky, R. Holzwarth, and T. J. Kippenberg, “Frequency comb assisted diode laser spectroscopy for measurement of microcavity dispersion,” *Nat. Photonics*, vol. 3, no. 9, pp. 529–533, 2009.

[30] M. Giunta, M. Fischer, W. Hänsel, T. Steinmetz, M. Lessing, S. Holzberger, C. Cleff, T. W. Hänsch, M. Mei, and R. Holzwarth, “20 years and 20 decimal digits: A journey with optical frequency combs,” *IEEE Photonics Technology Letters*, vol. 31, no. 23, pp. 1898–1901, 2019.

[31] T. W. Hänsch, “Nobel lecture: passion for precision,” *Rev. Mod. Phys.*, vol. 78, no. 4, p. 1297, 2006.

[32] D. J. Jones, S. A. Diddams, J. K. Ranka, A. Stentz, R. S. Windeler, J. L. Hall, and S. T. Cundiff, “Carrier-envelope phase control of femtosecond mode-locked lasers and direct optical frequency synthesis,” *Science*, vol. 288, no. 5466, pp. 635–639, 2000.

[33] R. Holzwarth, T. Udem, T. W. Hänsch, J. Knight, W. Wadsworth, and P. S. J. Russell, “Optical frequency synthesizer for precision spectroscopy,” *Phys. Rev. Lett.*, vol. 85, no. 11, p. 2264, 2000.

[34] P. Del’Haye, A. Schliesser, O. Arcizet, T. Wilken, R. Holzwarth, and T. J. Kippenberg, “Optical frequency comb generation from a monolithic microresonator,” *Nature*, vol. 450, no. 7173, pp. 1214–1217, 2007.

[35] H. Schnatz, B. Lipphardt, J. Helmcke, F. Riehle, and G. Zinner, “First phase-coherent frequency measurement of visible radiation,” *Phys. Rev. Lett.*, vol. 76, no. 1, p. 18, 1996.

[36] P. F. Moulton, “Spectroscopic and laser characteristics of Ti: Al_2O_3,” *JOSA B*, vol. 3, no. 1, pp. 125–133, 1986.

[37] D. E. Spence, P. N. Kean, and W. Sibbett, “60-fsec pulse generation from a self-mode-locked Ti:sapphire laser,” *Opt. Lett.*, vol. 16, no. 1, pp. 42–44, 1991.

[38] T. Nakamura, J. Davila-Rodriguez, H. Leopardi, J. A. Sherman, T. M. Fortier, X. Xie, J. C. Campbell, W. F. McGrew, X. Zhang, Y. S. Hassan, Nicolodi, B. Daniele, L. Kyle, D. Andrew D., Q. Scott A., and Franklyn, “Coherent optical clock down-conversion for microwave frequencies with 10^{-18} instability,” *Science*, vol. 368, no. 6493, pp. 889–892, 2020.

[39] T. Udem, R. Holzwarth, and T. W. Hänsch, “Optical frequency metrology,” *Nature*, vol. 416, no. 6877, pp. 233–237, 2002.

[40] T. Fortier and E. Baumann, “20 years of developments in optical frequency comb technology and applications,” *Commun. Phys.*, vol. 2, no. 1, pp. 1–16, 2019.

[41] S. A. Diddams, K. Vahala, and T. Udem, “Optical frequency combs: Coherently uniting the electromagnetic spectrum,” *Science*, vol. 369, no. 6501, p. eaay3676, 2020.

[42] R. Zhuang, K. Ni, G. Wu, T. Hao, L. Lu, Y. Li, and Q. Zhou, “Electro-optic frequency combs: Theory, characteristics, and applications,” *Laser & Photonics Reviews*, p. 2200353.

[43] H. Murata, A. Morimoto, T. Kobayashi, and S. Yamamoto, “Optical pulse generation by electrooptic-modulation method and its application to integrated ultrashort pulse generators,” *IEEE J. Sel. Top. Quantum Electron.*, vol. 6, no. 6, pp. 1325–1331, 2000.

[44] D. R. Carlson, D. D. Hickstein, W. Zhang, A. J. Metcalf, F. Quinlan, S. A. Diddams, and S. B. Papp, “Ultrafast electro-optic light with subcycle control,” *Science*, vol. 361, no. 6409, pp. 1358–1363, 2018.

[45] V. Torres-Company and A. M. Weiner, "Optical frequency comb technology for ultra-broadband radio-frequency photonics," *Laser Photon. Rev.*, vol. 8, no. 3, pp. 368–393, 2014.

[46] A. J. Metcalf, V. Torres-Company, D. E. Leaird, and A. M. Weiner, "High-power broadly tunable electrooptic frequency comb generator," *IEEE J Sel Top Quantum Electron.*, vol. 19, no. 6, pp. 231–236, 2013.

[47] A. Pasquazi, M. Peccianti, L. Razzari, D. J. Moss, S. Coen, M. Erkintalo, Y. K. Chembo, T. Hansson, S. Wabnitz, P. Del'Haye, Xue, W. Xiaoxiao, M. Andrew M., and Roberto, "Micro-combs: A novel generation of optical sources," *Phys. Rep.*, vol. 729, pp. 1–81, 2018.

[48] E. Cartlidge, "Combs of light on a chip," *Optics and Photonics News*, vol. 32, no. 1, pp. 26–33, 2021.

[49] Q.-F. Yang, M.-G. Suh, K. Y. Yang, X. Yi, and K. J. Vahala, "Microresonator soliton dual-comb spectroscopy," in *CLEO: Science and Innovations.* Optical Society of America, 2017, pp. SM4D–4.

[50] P. Marin-Palomo, J. N. Kemal, M. Karpov, A. Kordts, J. Pfeifle, M. H. Pfeiffer, P. Trocha, S. Wolf, V. Brasch, M. H. Anderson, R. Rosenberger, K. Vijayan, W. Freude, T. J. Kippenberg, and C. Koos, "Microresonator-based solitons for massively parallel coherent optical communications," *Nature*, vol. 546, no. 7657, pp. 274–279, 2017.

[51] A. Fülöp, M. Mazur, A. Lorences-Riesgo, Ó. B. Helgason, P.-H. Wang, Y. Xuan, D. E. Leaird, M. Qi, P. A. Andrekson, A. M. Weiner, and V. Torres-Company, "High-order coherent communications using mode-locked dark-pulse Kerr combs from microresonators," *Nat. Commun.*, vol. 9, no. 1, p. 1598, 2018.

[52] S. B. Papp, K. Beha, P. Del'Haye, F. Quinlan, H. Lee, K. J. Vahala, and S. A. Diddams, "Microresonator frequency comb optical clock," *Optica*, vol. 1, no. 1, pp. 10–14, 2014.

[53] D. T. Spencer, T. Drake, T. C. Briles, J. Stone, L. C. Sinclair, C. Fredrick, Q. Li, D. Westly, B. R. Ilic, A. Bluestone, N. Volet, T. Komljenovic, L. Chang, S. H. Lee, D. Y. Oh, M.-G. Suh, K. Y. Yang, M. H. P. Pfeiffer, T. J. Kippenberg, E. Norberg, L. Theogarajan, K. Vahala, N. R. Newbury, K. Srinivasan, J. E. Bowers,

S. A. Diddams, and S. B. Papp, “An optical-frequency synthesizer using integrated photonics,” *Nature*, vol. 557, no. 7703, pp. 81–85, 2018.

[54] T. Kippenberg, S. Spillane, and K. Vahala, “Kerr-nonlinearity optical parametric oscillation in an ultrahigh-Q toroid microcavity,” *Phys. Rev. Lett.*, vol. 93, no. 8, p. 083904, 2004.

[55] P. Del’Haye, O. Arcizet, A. Schliesser, R. Holzwarth, and T. J. Kippenberg, “Full stabilization of a microresonator-based optical frequency comb,” *Phys. Rev. Lett.*, vol. 101, no. 5, p. 053903, 2008.

[56] L. Razzari, D. Duchesne, M. Ferrera, R. Morandotti, S. Chu, B. E. Little, and D. J. Moss, “Cmos-compatible integrated optical hyper-parametric oscillator,” *Nature Photonics*, vol. 4, no. 1, pp. 41–45, 2010.

[57] T. Herr, V. Brasch, J. D. Jost, C. Y. Wang, N. M. Kondratiev, M. L. Gorodetsky, and T. J. Kippenberg, “Temporal solitons in optical microresonators,” *Nat. Photonics*, vol. 8, no. 2, pp. 145–152, 2014.

[58] T. J. Kippenberg, A. L. Gaeta, M. Lipson, and M. L. Gorodetsky, “Dissipative Kerr solitons in optical microresonators,” *Science*, vol. 361, no. 6402, p. eaan8083, 2018.

[59] E. Nazemosadat, A. Fülöp, Ó. B. Helgason, P.-H. Wang, Y. Xuan, D. E. Leaird, M. Qi, E. Silvestre, A. M. Weiner, and V. Torres-Company, “Switching dynamics of dark-pulse Kerr frequency comb states in optical microresonators,” *Phys. Rev. A*, vol. 103, no. 1, p. 013513, 2021.

[60] V. Lobanov, G. Lihachev, T. Kippenberg, and M. Gorodetsky, “Frequency combs and platicons in optical microresonators with normal GVD,” *Opt. Express*, vol. 23, no. 6, pp. 7713–7721, 2015.

[61] P. Del’Haye, A. Coillet, W. Loh, K. Beha, S. B. Papp, and S. A. Diddams, “Phase steps and resonator detuning measurements in microresonator frequency combs,” *Nat. Commun.*, vol. 6, no. 1, p. 5668, 2015.

[62] S. T. Cundiff and A. M. Weiner, “Optical arbitrary waveform generation,” *Nat. Photonics*, vol. 4, no. 11, pp. 760–766, 2010.

[63] B. L. Danielson, “Optical time-domain reflectometer specifications and performance testing,” *Appl. Opt.*, vol. 24, no. 15, pp. 2313–2322, 1985.

[64] B. R. Masters, “Early development of optical low-coherence reflectometry and some recent biomedical applications,” *J. Biomed. Opt.*, vol. 4, no. 2, pp. 236–247, 1999.

[65] R. C. Youngquist, S. Carr, and D. E. Davies, “Optical coherence-domain reflectometry: a new optical evaluation technique,” *Opt. Lett.*, vol. 12, no. 3, pp. 158–160, 1987.

[66] D. Huang, E. A. Swanson, C. P. Lin, J. S. Schuman, W. G. Stinson, W. Chang, M. R. Hee, T. Flotte, K. Gregory, C. A. Puliafito, and J. G. Fujimoto, “Optical coherence tomography,” *Science*, vol. 254, no. 5035, pp. 1178–1181, 1991.

[67] B. J. Soller, D. K. Gifford, M. S. Wolfe, and M. E. Froggatt, “High resolution optical frequency domain reflectometry for characterization of components and assemblies,” *Opt. Express*, vol. 13, no. 2, pp. 666–674, 2005.

[68] P. Chaisakul, D. Marris-Morini, J. Frigerio, D. Chrastina, M.-S. Rouifed, S. Cecchi, P. Crozat, G. Isella, and L. Vivien, “Integrated germanium optical interconnects on silicon substrates,” *Nat. Photonics*, vol. 8, no. 6, pp. 482–488, 2014.

[69] S.-H. Yun, G. J. Tearney, J. F. de Boer, N. Iftimia, and B. E. Bouma, “High-speed optical frequency-domain imaging,” *Opt. Express*, vol. 11, no. 22, pp. 2953–2963, 2003.

[70] M. Froggatt and J. Moore, “High-spatial-resolution distributed strain measurement in optical fiber with Rayleigh scatter,” *Appl. Opt.*, vol. 37, no. 10, pp. 1735–1740, 1998.

[71] W. Eickhoff and R. Ulrich, “Optical frequency domain reflectometry in single-mode fiber,” *Appl. Phys. Lett.*, vol. 39, no. 9, pp. 693–695, 1981.

[72] S. Personick, “Photon probe—an optical-fiber time-domain reflectometer,” *Bell Syst. Tech. J.*, vol. 56, no. 3, pp. 355–366, 1977.

[73] M. Barnoski, M. Rourke, S. Jensen, and R. Melville, “Optical time domain reflectometer,” *Appl. Opt.*, vol. 16, no. 9, pp. 2375–2379, 1977.

[74] E. D. Moore, “Advances in swept-wavelength interferometry for precision measurements,” Ph.D. dissertation, University of Colorado at Boulder, 2011.

[75] P. A. Roos, R. R. Reibel, T. Berg, B. Kaylor, Z. W. Barber, and W. R. Babbitt, “Ultrabroadband optical chirp linearization for precision metrology applications,” *Opt. Lett.*, vol. 34, no. 23, pp. 3692–3694, 2009.

[76] K. Iiyama, L.-T. Wang, and K.-I. Hayashi, “Linearizing optical frequency-sweep of a laser diode for FMCW reflectometry,” *J. Lightwave Technol.*, vol. 14, no. 2, pp. 173–178, 1996.

[77] U. Glombitza and E. Brinkmeyer, “Coherent frequency-domain reflectometry for characterization of single-mode integrated-optical waveguides,” *J. Lightwave Technol.*, vol. 11, no. 8, pp. 1377–1384, 1993.

[78] E. D. Moore and R. R. McLeod, “Correction of sampling errors due to laser tuning rate fluctuations in swept-wavelength interferometry,” *Opt. Express*, vol. 16, no. 17, pp. 13 139–13 149, 2008.

[79] S. Fujii and T. Tanabe, “Dispersion engineering and measurement of whispering gallery mode microresonator for Kerr frequency comb generation,” *Nanophotonics*, vol. 9, no. 5, pp. 1087–1104, 2020.

[80] E. Baumann, F. R. Giorgetta, I. Coddington, L. C. Sinclair, K. Knabe, W. C. Swann, and N. R. Newbury, “Comb-calibrated frequency-modulated continuous-wave ladar for absolute distance measurements,” *Opt. Lett.*, vol. 38, no. 12, pp. 2026–2028, 2013.

[81] W. Yu, P. Pfeiffer, A. Morsali, J. Yang, and J. Fontaine, “Comb-calibrated frequency sweeping interferometry for absolute distance and vibration measurement,” *Opt. Lett.*, vol. 44, no. 20, pp. 5069–5072, 2019.

[82] E. Baumann, F. R. Giorgetta, J.-D. Deschênes, W. C. Swann, I. Coddington, and N. R. Newbury, “Comb-calibrated laser ranging

for three-dimensional surface profiling with micrometer-level precision at a distance," *Opt. Express*, vol. 22, no. 21, pp. 24 914–24 928, 2014.

[83] J. Liu, V. Brasch, M. H. Pfeiffer, A. Kordts, A. N. Kamel, H. Guo, M. Geiselmann, and T. J. Kippenberg, "Frequency-comb-assisted broadband precision spectroscopy with cascaded diode lasers," *Opt. Lett.*, vol. 41, no. 13, pp. 3134–3137, 2016.

[84] C. A. Rosiek, G. Arregui, A. Vladimirova, M. Albrechtsen, B. Vosoughi Lahijani, R. E. Christiansen, and S. Stobbe, "Observation of strong backscattering in valley-hall photonic topological interface modes," *Nat. Photonics*, pp. 1–7, 2023.

[85] G. Tittelbach, B. Richter, and W. Karthe, "Comparison of three transmission methods for integrated optical waveguide propagation loss measurement," *J. Opt. Pure Appl. Opt.*, vol. 2, no. 6, p. 683, 1993.

[86] J. F. Bauters, M. J. Heck, D. John, D. Dai, M.-C. Tien, J. S. Barton, A. Leinse, R. G. Heideman, D. J. Blumenthal, and J. E. Bowers, "Ultra-low-loss high-aspect-ratio Si_3N_4 waveguides," *Opt. Express*, vol. 19, no. 4, pp. 3163–3174, 2011.

[87] M. Melchiorri, N. Daldosso, F. Sbrana, L. Pavesi, G. Pucker, C. Kompocholis, P. Bellutti, and A. Lui, "Propagation losses of silicon nitride waveguides in the near-infrared range," *Appl. Phys. Lett.*, vol. 86, no. 12, p. 121111, 2005.

[88] R. Adar, M. Serbin, and V. Mizrahi, "Less than 1 dB per meter propagation loss of silica waveguides measured using a ring resonator," *J. Lightwave Technol.*, vol. 12, no. 8, pp. 1369–1372, 1994.

[89] P. Rabiei, W. H. Steier, C. Zhang, and L. R. Dalton, "Polymer micro-ring filters and modulators," *J. Lightwave Technol.*, vol. 20, no. 11, p. 1968, 2002.

[90] S. Spillane, T. Kippenberg, O. Painter, and K. Vahala, "Ideality in a fiber-taper-coupled microresonator system for application to cavity quantum electrodynamics," *Phys. Rev. Lett.*, vol. 91, no. 4, p. 043902, 2003.

[91] R. MacDonald, "Frequency domain optical reflectometer," *Appl. Opt.*, vol. 20, no. 10, pp. 1840–1844, 1981.

[92] J. Von Der Weid, R. Passy, G. Mussi, and N. Gisin, "On the characterization of optical fiber network components with optical frequency domain reflectometry," *J. Lightwave Technol.*, vol. 15, no. 7, pp. 1131–1141, 1997.

[93] M. Badar, P. Lu, M. Buric, and P. Ohodnicki Jr, "Integrated auxiliary interferometer for self-correction of nonlinear tuning in optical frequency domain reflectometry," *J. Lightwave Technol.*, vol. 38, no. 21, pp. 6097–6103, 2020.

[94] K. Twayana, Z. Ye, Ó. B. Helgason, K. Vijayan, M. Karlsson *et al.*, "Frequency-comb-calibrated swept-wavelength interferometry," *Opt. Express*, vol. 29, no. 15, pp. 24 363–24 372, 2021.

[95] J. F. Bauters, M. J. Heck, D. D. John, J. S. Barton, C. M. Bruinink, A. Leinse, R. G. Heideman, D. J. Blumenthal, and J. E. Bowers, "Planar waveguides with less than 0.1 dB/m propagation loss fabricated with wafer bonding," *Opt. Express*, vol. 19, no. 24, pp. 24 090–24 101, 2011.

[96] L. A. Bru, D. Pastor, and P. Muñoz, "Integrated optical frequency domain reflectometry device for characterization of complex integrated devices," *Opt. Express*, vol. 26, no. 23, pp. 30 000–30 008, 2018.

[97] X. Zhang, Y. Yin, X. Yin, Y. Wen, X. Zhang, X. Liu, and H. Lv, "Characterizing microring resonators using optical frequency domain reflectometry," *Opt. Lett.*, vol. 46, no. 10, pp. 2400–2403, 2021.

[98] J.-P. von der Weid, R. Passy, and N. Gisin, "Mid-range coherent optical frequency domain reflectometry with a DFB laser diode coupled to an external cavity," *J. Lightwave Technol.*, vol. 13, no. 5, pp. 954–960, 1995.

[99] A. Weiner, *Ultrafast optics.* John Wiley & Sons, 2011.

[100] Z. Ye, P. Zhao, K. Twayana, M. Karlsson, P. A. Andrekson, and V. Torres-Company, "Ultralow-loss meter-long dispersion-engineered silicon nitride waveguides," in *2021 Conference on Lasers and Electro-Optics (CLEO).* IEEE, 2021, paper SF1C.5.

[101] Z. Ye, P. Zhao, K. Twayana, M. Karlsson, V. Torres-Company, and P. A. Andrekson, “Overcoming the quantum limit of optical amplification in monolithic waveguides,” *Sci. Adv.*, vol. 7, no. 38, p. eabi8150, 2021.

[102] Z. Ye, “Ultralow-loss silicon nitride waveguides for nonlinear optics,” Ph.D. dissertation, Chalmers Tekniska Hogskola (Sweden), 2021.

[103] A. Perot and C. Fabry, “On the application of interference phenomena to the solution of various problems of spectroscopy and metrology,” *Astrophysical Journal, vol. 9, p. 87*, vol. 9, p. 87, 1899.

[104] G. Liang, H. Huang, A. Mohanty, M. C. Shin, X. Ji, M. J. Carter, S. Shrestha, M. Lipson, and N. Yu, “Robust, efficient, micrometre-scale phase modulators at visible wavelengths,” *Nat. Photonics*, vol. 15, no. 12, pp. 908–913, 2021.

[105] C. K. Madsen and J. H. Zhao, *Optical filter design and analysis*. Wiley New York, 1999.

[106] S. Yang, Y. Wang, and H. Sun, “Advances and prospects for whispering gallery mode microcavities,” *Advanced Optical Materials*, vol. 3, no. 9, pp. 1136–1162, 2015.

[107] W. Jin, Q.-F. Yang, L. Chang, B. Shen, H. Wang, M. A. Leal, L. Wu, M. Gao, A. Feshali, M. Paniccia *et al.*, “Hertz-linewidth semiconductor lasers using CMOS-ready ultra-high-Q microresonators,” *Nat. Photonics*, vol. 15, no. 5, pp. 346–353, 2021.

[108] C. Xiang, W. Jin, O. Terra, B. Dong, H. Wang, L. Wu, J. Guo, T. J. Morin, E. Hughes, J. Peters *et al.*, “Three-dimensional integration enables ultra-low-noise, isolator-free Si photonics,” *arXiv preprint arXiv:2301.09989*, 2023.

[109] J. Liu, E. Lucas, A. S. Raja, J. He, J. Riemensberger, R. N. Wang, M. Karpov, H. Guo, R. Bouchand, and T. J. Kippenberg, “Photonic microwave generation in the X-and K-band using integrated soliton microcombs,” *Nat. Photonics*, vol. 14, no. 8, pp. 486–491, 2020.

[110] A. Dutt, K. Luke, S. Manipatruni, A. L. Gaeta, P. Nussenzveig, and M. Lipson, “On-chip optical squeezing,” *Phys. Rev. Appl.*, vol. 3, no. 4, p. 044005, 2015.

[111] E. Marcatili, "Bends in optical dielectric guides," *Bell System Technical Journal*, vol. 48, no. 7, pp. 2103–2132, 1969.

[112] H. A. Haus and W. Huang, "Coupled-mode theory," *Proceedings of the IEEE*, vol. 79, no. 10, pp. 1505–1518, 1991.

[113] J. K. Poon, J. Scheuer, S. Mookherjea, G. T. Paloczi, Y. Huang, and A. Yariv, "Matrix analysis of microring coupled-resonator optical waveguides," *Opt. Express*, vol. 12, no. 1, pp. 90–103, 2004.

[114] A. Yariv, "Universal relations for coupling of optical power between microresonators and dielectric waveguides," *Electron. Lett.*, vol. 36, no. 4, pp. 321–322, 2000.

[115] Ó. B. Helgason, M. Girardi, Z. Ye, F. Lei, J. Schröder, and V. T. Company, "Power-efficient soliton microcombs," *arXiv preprint arXiv:2202.09410*, 2022.

[116] K. Twayana, Z. Ye, Ó. B. Helgason, M. Karlsson *et al.*, "Frequency-comb-assisted swept-wavelength interferometry," in *The European Conference on Lasers and Electro-Optics.* Optica Publishing Group, 2021, p. ch_10_6.

[117] W. Bogaerts, P. De Heyn, T. Van Vaerenbergh, K. De Vos, S. Kumar Selvaraja, T. Claes, P. Dumon, P. Bienstman, D. Van Thourhout, and R. Baets, "Silicon microring resonators," *Laser Photonics Rev.*, vol. 6, no. 1, pp. 47–73, 2012.

[118] Y. Xuan, Y. Liu, L. T. Varghese, A. J. Metcalf, X. Xue, P.-H. Wang, K. Han, J. A. Jaramillo-Villegas, A. Al Noman, C. Wang *et al.*, "High-Q silicon nitride microresonators exhibiting low-power frequency comb initiation," *Optica*, vol. 3, no. 11, pp. 1171–1180, 2016.

[119] J. K. Poon, J. Scheuer, Y. Xu, and A. Yariv, "Designing coupled-resonator optical waveguide delay lines," *JOSA B*, vol. 21, no. 9, pp. 1665–1673, 2004.

[120] C. R. Pollock and M. Lipson, *Integrated photonics.* Springer, 2003, vol. 20, no. 25.

[121] M. Dahlem, "Studies of advanced integrated nano-photonic devices in silicon," Ph.D. dissertation, Massachusetts Institute of Technology, 2011.

[122] B. E. Little, S. T. Chu, H. A. Haus, J. Foresi, and J.-P. Laine, "Microring resonator channel dropping filters," *J. Lightwave Technol.*, vol. 15, no. 6, pp. 998–1005, 1997.

[123] A. Li, T. Van Vaerenbergh, P. De Heyn, P. Bienstman, and W. Bogaerts, "Backscattering in silicon microring resonators: a quantitative analysis," *Laser Photonics Rev.*, vol. 10, no. 3, pp. 420–431, 2016.

[124] M. H. Pfeiffer, J. Liu, A. S. Raja, T. Morais, B. Ghadiani, and T. J. Kippenberg, "Ultra-smooth silicon nitride waveguides based on the damascene reflow process: fabrication and loss origins," *Optica*, vol. 5, no. 7, pp. 884–892, 2018.

[125] Q. Li, A. A. Eftekhar, Z. Xia, and A. Adibi, "Unified approach to mode splitting and scattering loss in high-Q whispering-gallery-mode microresonators," *Phys. Rev. A*, vol. 88, no. 3, p. 033816, 2013.

[126] Ó. B. Helgason, F. R. Arteaga-Sierra, Z. Ye, K. Twayana, P. A. Andrekson, M. Karlsson, J. Schröder, and V. Torres-Company, "Dissipative solitons in photonic molecules," *Nat. Photonics*, vol. 15, no. 4, pp. 305–310, 2021.

[127] S. V. Boriskina, "Photonic molecules and spectral engineering," *Photonic microresonator research and applications*, pp. 393–421, 2010.

[128] X. Xue, Y. Xuan, Y. Liu, P.-H. Wang, S. Chen, J. Wang, D. E. Leaird, M. Qi, and A. M. Weiner, "Mode-locked dark pulse Kerr combs in normal-dispersion microresonators," *Nat. Photonics*, vol. 9, no. 9, pp. 594–600, 2015.

[129] T. Herr, V. Brasch, J. Jost, I. Mirgorodskiy, G. Lihachev, M. Gorodetsky, and T. Kippenberg, "Mode spectrum and temporal soliton formation in optical microresonators," *Phys. Rev. Lett.*, vol. 113, no. 12, p. 123901, 2014.

[130] J. Niehusmann, A. Vörckel, P. H. Bolivar, T. Wahlbrink, W. Henschel, and H. Kurz, "Ultrahigh-quality-factor silicon-on-insulator microring resonator," *Opt. Lett.*, vol. 29, no. 24, pp. 2861–2863, 2004.

[131] W. McKinnon, D.-X. Xu, C. Storey, E. Post, A. Densmore, A. Delâge, P. Waldron, J. Schmid, and S. Janz, "Extracting coupling and loss coefficients from a ring resonator," *Opt. Express*, vol. 17, no. 21, pp. 18 971–18 982, 2009.

[132] J. E. Heebner, V. Wong, A. Schweinsberg, R. W. Boyd, and D. J. Jackson, "Optical transmission characteristics of fiber ring resonators," *IEEE J. Quantum Electron.*, vol. 40, no. 6, pp. 726–730, 2004.

[133] K. Wu and A. W. Poon, "Stress-released Si_3N_4 fabrication process for dispersion-engineered integrated silicon photonics," *Opt. Express*, vol. 28, no. 12, pp. 17 708–17 722, 2020.

[134] V. Brasch, M. Geiselmann, T. Herr, G. Lihachev, M. H. Pfeiffer, M. L. Gorodetsky, and T. J. Kippenberg, "Photonic chip–based optical frequency comb using soliton cherenkov radiation," *Science*, vol. 351, no. 6271, pp. 357–360, 2016.

[135] M. H. Pfeiffer, C. Herkommer, J. Liu, H. Guo, M. Karpov, E. Lucas, M. Zervas, and T. J. Kippenberg, "Octave-spanning dissipative Kerr soliton frequency combs in Si_3N_4 microresonators," *Optica*, vol. 4, no. 7, pp. 684–691, 2017.

[136] F. Ferdous, H. Miao, D. E. Leaird, K. Srinivasan, J. Wang, L. Chen, L. T. Varghese, and A. M. Weiner, "Spectral line-by-line pulse shaping of on-chip microresonator frequency combs," *Nat. Photonics*, vol. 5, no. 12, pp. 770–776, 2011.

[137] K. Ikeda, R. E. Saperstein, N. Alic, and Y. Fainman, "Thermal and Kerr nonlinear properties of plasma-deposited silicon nitride/silicon dioxide waveguides," *Opt. Express*, vol. 16, no. 17, pp. 12 987–12 994, 2008.

[138] G. P. Agrawal, "Nonlinear fiber optics," in *Nonlinear Science at the Dawn of the 21st Century.* Springer, 2000, pp. 195–211.

[139] K. Ikeda, "Multiple-valued stationary state and its instability of the transmitted light by a ring cavity system," *Opt. Commun.*, vol. 30, no. 2, pp. 257–261, 1979.

[140] L. A. Lugiato and R. Lefever, "Spatial dissipative structures in passive optical systems," *Phys. Rev. Lett.*, vol. 58, no. 21, p. 2209, 1987.

[141] M. Haelterman, S. Trillo, and S. Wabnitz, "Dissipative modulation instability in a nonlinear dispersive ring cavity," *Opt. Commun.*, vol. 91, no. 5-6, pp. 401–407, 1992.

[142] T. Hansson, D. Modotto, and S. Wabnitz, "Dynamics of the modulational instability in microresonator frequency combs," *Phys. Rev. A*, vol. 88, no. 2, p. 023819, 2013.

[143] S. Coen and M. Erkintalo, "Universal scaling laws of Kerr frequency combs," *Opt. Lett.*, vol. 38, no. 11, pp. 1790–1792, 2013.

[144] J. A. Jaramillo-Villegas, X. Xue, P.-H. Wang, D. E. Leaird, and A. M. Weiner, "Deterministic single soliton generation and compression in microring resonators avoiding the chaotic region," *Opt. Express*, vol. 23, no. 8, pp. 9618–9626, 2015.

[145] A. Fülöp, *Fiber-optic communications with microresonator frequency combs.* Chalmers Tekniska Hogskola (Sweden), 2018.

[146] V. Torres-Company, D. Castelló-Lurbe, and E. Silvestre, "Comparative analysis of spectral coherence in microresonator frequency combs," *Opt. Express*, vol. 22, no. 4, pp. 4678–4691, 2014.

[147] X. Xue, Y. Xuan, P.-H. Wang, Y. Liu, D. E. Leaird, M. Qi, and A. M. Weiner, "Normal-dispersion microcombs enabled by controllable mode interactions," *Laser Photonics Rev.*, vol. 9, no. 4, pp. L23–L28, 2015.

[148] S. Wabnitz, "Suppression of interactions in a phase-locked soliton optical memory," *Opt. Lett.*, vol. 18, no. 8, pp. 601–603, 1993.

[149] H. Guo, M. Karpov, E. Lucas, A. Kordts, M. H. Pfeiffer, V. Brasch, G. Lihachev, V. E. Lobanov, M. L. Gorodetsky, and T. J. Kippenberg, "Universal dynamics and deterministic switching of dissipative Kerr solitons in optical microresonators," *Nat. Physics*, vol. 13, no. 1, pp. 94–102, 2017.

[150] C. Joshi, J. K. Jang, K. Luke, X. Ji, S. A. Miller, A. Klenner, Y. Okawachi, M. Lipson, and A. L. Gaeta, "Thermally controlled comb generation and soliton modelocking in microresonators," *Opt. Lett.*, vol. 41, no. 11, pp. 2565–2568, 2016.

[151] P.-H. Wang, J. A. Jaramillo-Villegas, Y. Xuan, X. Xue, C. Bao, D. E. Leaird, M. Qi, and A. M. Weiner, "Intracavity characterization of micro-comb generation in the single-soliton regime," *Opt. Express*, vol. 24, no. 10, pp. 10 890–10 897, 2016.

[152] Y. H. Wen, M. R. Lamont, S. H. Strogatz, and A. L. Gaeta, "Self-organization in Kerr-cavity-soliton formation in parametric frequency combs," *Phys. Rev. A*, vol. 94, no. 6, p. 063843, 2016.

[153] Z. Jiang, D. E. Leaird, and A. M. Weiner, "Optical arbitrary waveform generation and characterization using spectral line-by-line control," *J. Lightwave Technol.*, vol. 24, no. 7, pp. 2487–2494, 2006.

[154] D. J. Kane and R. Trebino, "Characterization of arbitrary femtosecond pulses using frequency-resolved optical gating," *IEEE J. Quantum Electron.*, vol. 29, no. 2, pp. 571–579, 1993.

[155] C. Iaconis and I. A. Walmsley, "Spectral phase interferometry for direct electric-field reconstruction of ultrashort optical pulses," *Opt. Lett.*, vol. 23, no. 10, pp. 792–794, 1998.

[156] J. Armstrong, "Measurement of picosecond laser pulse widths," *Appl. Phys. Lett.*, vol. 10, no. 1, pp. 16–18, 1967.

[157] K. Chu, J. Heritage, R. Grant, K. Liu, A. Dienes, W. White, and A. Sullivan, "Direct measurement of the spectral phase of femtosecond pulses," *Opt. Lett.*, vol. 20, no. 8, pp. 904–906, 1995.

[158] P. Kockaert, M. Peeters, S. Coen, P. Emplit, M. Haelterman, and O. Deparis, "Simple amplitude and phase measuring technique for ultrahigh-repetition-rate lasers," *IEEE Photonics Technol. Lett.*, vol. 12, no. 2, pp. 187–189, 2000.

[159] D. Reid, S. Murdoch, and L. Barry, "Stepped-heterodyne optical complex spectrum analyzer." *Opt. Express*, vol. 18, no. 19, pp. 19 724–19 731, 2010.

[160] M. Korti, T. Habruseva, S. Slepneva, K. Merghem, G. Huyet, Y. Gottesman, A. Ramdane, B.-E. Benkelfat, and O. Seddiki, "Fast-recovery of the amplitude and phase of short optical pulses using a frequency-swept source based heterodyne measurement," *IEEE Photon. J.*, vol. 10, no. 3, pp. 1–7, 2018.

[161] B. Szafraniec and D. M. Baney, "Swept coherent spectrum analysis of the complex optical field," in *Proceedings of the Lightwave Technologies in Instrumentation and Measurement Conference.* IEEE, 2004, pp. 68–72.

[162] F. Ferdous, D. E. Leaird, C.-B. Huang, and A. Weiner, "Dual-comb electric-field cross-correlation technique for optical arbitrary waveform characterization," *Opt. Lett.*, vol. 34, no. 24, pp. 3875–3877, 2009.

[163] A. Tikan, J. Riemensberger, K. Komagata, S. Hönl, M. Churaev, C. Skehan, H. Guo, R. N. Wang, J. Liu, P. Seidler, and T. J. Kippenberg, "Emergent nonlinear phenomena in a driven dissipative photonic dimer," *Nat. Phys.*, vol. 17, no. 5, pp. 604–610, 2021.

[164] D. C. Cole, E. S. Lamb, P. Del'Haye, S. A. Diddams, and S. B. Papp, "Soliton crystals in Kerr resonators," *Nat. Photonics*, vol. 11, no. 10, pp. 671–676, 2017.

[165] Z. Kong, C. Bao, O. E. Sandoval, B. Liu, C. Wang, J. A. Jaramillo-Villegas, M. Qi, and A. M. Weiner, "Characterizing pump line phase offset of a single-soliton Kerr comb by dual comb interferometry," *Opt. Lett.*, vol. 44, no. 6, pp. 1460–1463, 2019.

[166] S. G. Murdoch, R. T. Watts, Y. Xu, R. Maldonado-Basilio, J. Parra-Cetina, S. Latkowski, P. Landais, and L. P. Barry, "Spectral amplitude and phase measurement of a 40 GHz free-running quantum-dash modelocked laser diode," *Opt. Express*, vol. 19, no. 14, pp. 13 628–13 635, 2011.

[167] I. Coddington, W. C. Swann, and N. R. Newbury, "Coherent multiheterodyne spectroscopy using stabilized optical frequency combs," *Phys. Rev. Lett.*, vol. 100, no. 1, p. 013902, 2008.

[168] T. Butler, B. Tykalewicz, D. Goulding, B. Kelleher, G. Huyet, and S. Hegarty, "Reconstruction of dynamical pulse trains via time-resolved multiheterodyne detection," *Opt. Express*, vol. 21, no. 24, pp. 29 109–29 119, 2013.

[169] J. Davila-Rodriguez, M. Bagnell, C. Williams, and P. J. Delfyett, "Multiheterodyne detection for spectral compression and downconversion of arbitrary periodic optical signals," *J. Lightwave Technol.*, vol. 29, no. 20, pp. 3091–3098, 2011.

[170] N. K. Fontaine, D. J. Geisler, R. P. Scott, and S. Yoo, "Simultaneous and self-referenced amplitude and phase measurement of two frequency combs using multi-heterodyne spectroscopy," in *OFC/NFOEC*. IEEE, 2012, paper OW1C.1.

[171] X. Yi, Q.-F. Yang, K. Y. Yang, and K. Vahala, "Imaging soliton dynamics in optical microcavities," *Nat. Commun.*, vol. 9, no. 1, p. 3565, 2018.

Included papers A-E

Paper A

Krishna Twayana, Zhichao Ye, Óskar B. Helgason, Vijayan Kovendhan, Magnus Karlsson and Victor Torres-Company, “Frequency-comb-calibrated swept-wavelength interferometry”, *Optics Express*, 29, 15, 24363-24372, 2021.

Paper B

Krishna Twayana, Israel Rebolledo-Salgado, Ekaterina Deriushkina, Magnus Karlsson, Jochen Schröder and Victor Torres-Company, "Spectral Interferometry with Frequency Combs", *Micromachines*, 13, 4, 614, 2022.

Paper C

Fuchuan Lei, Zhichao Ye, Krishna Twayana, Yan Gao, Marcello Girardi, Óskar B. Helgason, Ping Zhao, and Victor Torres-Company, “Hyperparametric oscillation via bound states in the continuum”, *Physical Review Letters*, 130, 9, 09381, 2023.

Paper D

Krishna Twayana, Fuchuan Lei, Zhichao Ye, Israel Rebolledo-Salgado, Óskar B. Helgason, Magnus Karlsson, and Victor Torres-Company, “Differential phase reconstruction of microcombs”, *Optics Letters*, 47, 13, 3351-3354, 2022.

Paper E

Krishna Twayana, Israel Rebolledo-Salgado, Marcello Girardi, Fuchuan Lei, Óskar B. Helgason, Magnus Karlsson, and Victor Torres-Company, "Multi-heterodyne differential phase measurement of microcombs", *submitted to Conference on Lasers and Electro-Optics Europe*, 2023.